Investigation of pattern generating mechanisms during atrial fibrillation based on the FitzHugh Nagumo equations

Diploma thesis

Claudia Hamann
Fachgebiet Theoretische Physik II/Computational Physics
Institut für Physik
Fakultät für Mathematik und Naturwissenschaften
Technische Universität Ilmenau

Supervisor: Prof. Dr. Philipp Maaß

29. April 2008

Contents

List of Figures

List of Tables

1 Introduction

Heart diseases are the major death causes in the industrial world [1]. The normal pumping function of the heart is controlled and activated by electric impulses originating from a pacemaker source, normally the sinus node. These electric impulses, measurable as potential differences, propagate through the heart tissue by diffusive activation of neighbouring cells. A reduced function of the heart can have different causes like a lacking supply of the heart cells with blood or perturbations of the electrical activation pattern. In this work the electrical activation is studied. It depends on many different influences beginning with the regulation by the autonomous nervous system, the sinus node activity, conduction failures up to lagging responses of the cells to the activation due to, for example, a changed mineral balance or inflammation. Perturbations of the electrical activation system can be investigated by a description of the heart tissue as an excitable media. Various mathematical models of excitable media exist like the Hodgkin Huxley equations [2], which are derived especially for the impulse generation and propagation on nerve cells or the FitzHugh Nagumo (FHN) equations [3]. The FHN equations are used to describe excitable media in diverse fields as chemical reactions (e.g. the Bhelousov-Zhabotinsky reaction or the catalysis of carbon monoxide), population dynamics or epidemic spreads. Additionally they are a well-known and tested model for the impulse propagation and generation in nerve and heart cells. A feature of excitable media is the formation of spatio-temporal patterns of the characteristic variable of the system. These patterns give information about the system state. For heart diseases the spatio-temporal pattern of the electric potential represents the state of health of the heart tissue and the kind of underlying disease.

This work is focused on the investigation of spatio-temporal patterns, which are characteristic for atrial fibrillation. The fibrillatory state of the atria is often described by an irregular, chaotic pattern. The supposed origin is a relatively regular local source of activity as a spiral wave or ectopic focus. These sources lead to a perturbation of the propagation of the sinus node activations over the atrial tissue. Of particular interest are the conditions and mechanisms, leading to a fibrillatory state due to spiral waves or ectopic foci. By the use of the mathematical model one is able to numerically calculate the wavefront propagation to study the dependence of the occurrence of spiral waves, for example, on the properties of the heart tissue. With this knowledge it is possible to investigate interference of spiral waves with the wavefronts originating from the sinus node. Results of such a research can be compared to time series analysis of electrocardiogram recordings of patients suffering from atrial fibrillation or to experiments on atrial tissue.

The thesis will focus on the following questions:

- What are possible mechanisms or configurations yielding spiral wave patterns and ectopic foci?

- What are the characteristic properties of spiral waves and ectopic foci?

- Does an interference of a spiral wave or an ectopic focus and periodic generated wavefronts result in a fibrillatory state?

- What are the characteristic properties of this fibrillatory state?

To answer these questions, numerical calculations of the FitzHugh Nagumo equations are performed for different spatial distributions of the model parameters that describe the local cell properties. Phase diagrams are derived, which classify different states of heart dynamics in dependence of the control parameters. The dependence of the occurrence of local sources on the spatial parameter distribution is revealed in phase diagrams. Additionally, the properties of the spirals and the ectopic foci are determined. With this knowledge the interaction of a spiral wave with regular excitations is studied in a two-dimensional model of the atria for different pacing frequencies.

The thesis is organised as follows. In chapter 2 an introduction to atrial fibrillation is given and in chapter 3 the Hodgkin Huxley model is discussed, which describes electrical impulse generation along nerve cells by the cell membrane properties and ion channel conductivities. The simpler FitzHugh Nagumo model is derived by phase space analysis in section 3.3 and analysed in section 3.4. Chapter 4 gives an overview of configurations, which can generate spiral waves and fibrillatory patterns, as proposed in the literature and studied in previous investigations. Description and results of numerical calculations of more realistic scenarios are presented in chapter 5. Thereby, in section 5.2 the possibility to obtain ectopic activity by a spatial variation of the resting state stability is analysed and the properties of the obtained ectopic focus are presented. In section 5.3, mechanisms are investigated, which can generate spiral waves, their properties are discussed and a comparison with experimental studies of spiral waves is given. Finally, the interaction of a spiral wave with regular sinus node activations is studied in section 5.4. In the final chapter 6 the results and their implications are summarised and an outlook is given on prospective studies.

2　Atrial fibrillation

2.1　Definition and classification

Atrial fibrillation (AF) is the most common arrhythmia of the heart in clinical practice in the industrial countries. Approximately one-third of hospitalisations for cardiac disrhythms are caused by AF [4] and about 4.5 million people in the European Union have AF. The estimated prevalence lies between 4 out of 1000 people up to 100 out of 1000 people, increasing with the age of the person [5, 6] (see Figure 1). Since in the industrial countries the number of people older than 60 years is growing, the impact of AF will increase.
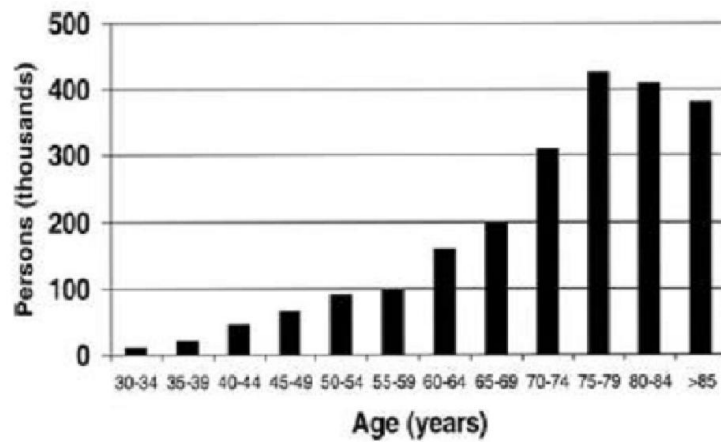
Figure 1: Prevalence vs. age of person (from [4]).

Atrial fibrillation is characterised by a fast irregular activation of the atria. During normal sinus rhythm the atria is paced by about 60 atrial beats per minute. In contrast, during AF the rate can increase up to 600 beats per minute. Short periods of AF can yield palpitations, chest discomfort and light-headedness. The uncoordinated activation leads to incomplete contraction of the atria, and, as a consequence, staining of blood. Hence thromboemboli can occur, which may propagate and lead to apoplectic stroke, pulmonary or other embolism. The risk for ischemic stroke is increased from two up to seven times for persons suffering from this disease [7]. Serious heart diseases can be promoted by AF as well. For example, sustained AF can cause severe congestive heart failures (CHF) after some time, which may be reversible, if the AF is treated with proper rate and/or rhythm control. Atrial fibrillation can not only promote other heart diseases. It is often also predisposed by several cardiac disorders, e.g. coronary artery disease, pericarditis, mitral valve disease, congenital heart disease, CHF, thyrotoxic heart disease and hypertension. These disorders are thought to assist AF by increasing the atrial pressure and/or by causing atrial dilations. But the precise links are still not known.
Dependent on whether AF is accompanied by other cardiac diseases, it can be divided into 'lone' (idiopathic) AF and sustained AF. The term 'lone' AF

is applied to patients under age 60 without clinical or echocardiographic evidence of heart disease, which exhibit normally a more favourable prognosis. Another classification criterion is the duration of fibrillation episodes of a certain patient. There exists acute (length < 24 hours) or chronic (recurrent) AF. Chronic AF is in turn divided into paroxysmal, persistent and permanent AF. Paroxysmal AF is characterised by self-terminating episodes (length < seven days), persistent AF by longer episodes, which can be stopped by cardioversion. If cardioversion failed, AF is termed permanent. The medical diagnosis and therapy are supported by a good classification of AF in the single case. On the other hand, different mechanisms are thought to generate and sustain the diverse classes of AF.

2.2 Theories about the mechanisms of atrial fibrillation

The electrical conduction system of the heart (see Figure 2) consists of:

- the sinus or sinoatrial node, placed in the upper part of the right atrium

- the atrioventricular (AV) node in the lower part of the right atrium

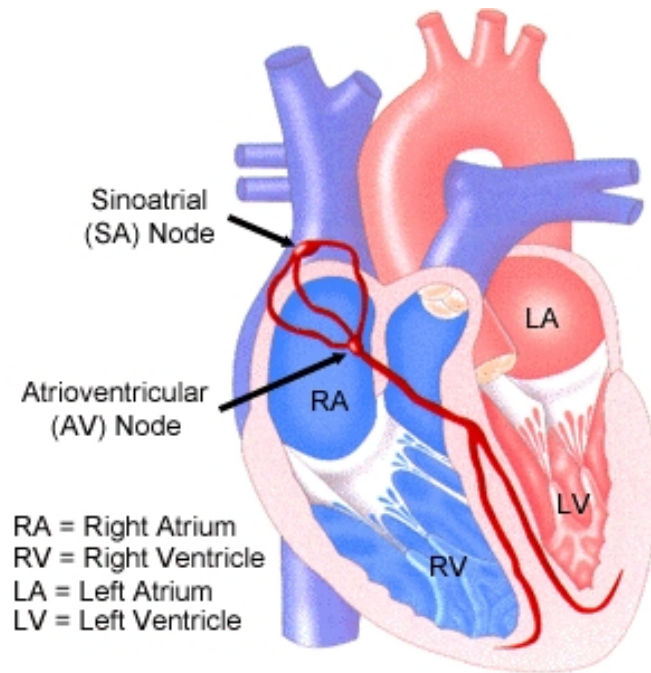- the bundle of His and the Purkinje fibres inside the septum between the ventricles.

Figure 2: The electrical conduction system of the heart (from [8]).

During a normal sinus rhythm the sinus node electrically activates the right atrium. This excitation travels orderly through the right atrium, excites the

left atrium and is then transferred to the ventricles through the AV node, the bundle of His and the Purkinje fibres. There the electrical activation leads to a contraction of the ventricles. The atria are paced by a frequency up to 12 Hz during AF. Although they are excited at this high rate, ventricular fibrillation is prevented by the filtering properties of the AV node. Every activation of the atria has to pass the AV node before being transferred to the ventricles. Hence, the effective 'heart rate'[1] is no longer controlled by the rhythm of the sinus node, but it is determined by the interaction of the atrial rate and the filtering properties of the AV node. The ventricular rate during AF is typically in the region of 150 beats per minute.

An important mechanism for the maintenance and recurrence of AF is the so called atrial remodelling. This means that the fibrillation itself alters the electrophysiological properties of the atria, which in return facilitates the occurrence of AF. The atrial remodelling has effects on the organ, cell and molecular level [9]. This changing of electrophysiological properties is a reason for the difficulties to distinguish between mechanisms generating and maintaining atrial fibrillation.

Different theories exist about the origin and the processes related with AF. They all describe the disturbed propagation of the electrical excitation through the atria. Three of them originate from the early twentieth century when AF was recognised and studied extensively. Mines [10] and Garrey [11] developed the idea that the fibrillation is maintained by multiple-simultaneous-reentrant circuits. These reentrant circuits should only be stable if the wave length of the excitation is shorter than the column of the muscle it appears on. The theory of a single, rapid atrial reentry circuit, often called 'mother wave', which produces irregular activation because of variable conduction through the atrial tissue[2] was evolved by Lewis [12]. Another concept is the atrial hyperexcitability first mentioned by Engelmann and Winterberg. Here, some cells of the atrium act as pacemaker and maintain in this way the arrhythmia. These pacemaker regions are called (rapidly discharging) ectopic foci. All three theories are schematically shown in Figure 3.

In 1962 Moe [14] developed the concept of the 'multiple wavelet hypothesis', which is more a quantitative refinement of the former theories than a new concept. It differs from the previous ones in that the reentry circuits do not have to return to their starting point. The propagation should rather involve multiple independent wavelets, which circulate around functionally refractory tissue. So they could extinguish themselves, if they reach a path of reduced excitability, or they propagate and maintain themselves and/or spawn daughter wavelets. Hence, if a sufficient number of wavelets could maintain themselves, the fibrillatory state is preserved.

Allesie *et al.* [15] performed mapping studies of atrial fibrillation in dog hearts, maintained by the presence of acetylcholine. Their results support the theory of Moe. Otherwise evidence emerged in some experiments for rapidly discharging ectopic foci in some clinical forms of AF [16], as well for the mother wave

---

[1] The effective 'heart rate' is the ventricular rate during AF.

[2] Some regions can not follow the high frequency of activation.
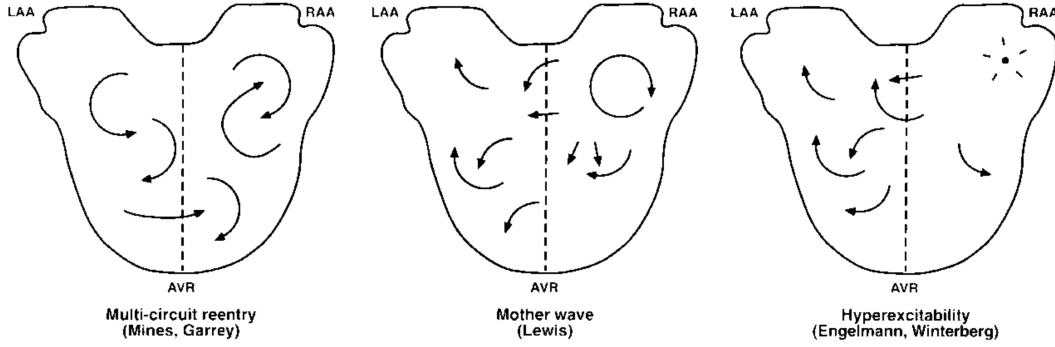
Figure 3: The three main hypotheses about the mechanisms generating and maintaining AF developed in the 1920s (from [13]).

theory as a mechanism of experimental AF [17, 18]. These results led to the conclusion that the three competing ideas about the mechanisms of AF can describe the fibrillatory state accurately in different situations.

Recent experiments [19, 20, 21] with high resolution optical mapping of AF reveal that the fibrillation is not that random as it is supposed by Moes theory. Furthermore a critical number of wavelets seems not to be essential for its maintenance. Some human studies [22, 23, 24, 25, 26, 27] and experiments [19, 20, 21, 28] indicate that local left atrial sources seem to play a more critical role for AF. Hence the hypothesis of Lewis, that a small number of stable reentrant circuits can maintain the fibrillatory state, is more consistent with the experimental results. From the experiments [26, 27] one can conclude that there are one or more stable pacemakers in the left atrium, which are generated by a stable spiral wave or ectopic foci. These lead to a chaotic, fibrillatory-like state through the propagation across the right atrium and the interaction with the sinus node. This theory is investigated using the FitzHugh Nagumo model in the following chapters.

3   Description of the model

The electrical excitation or activation, mentioned in the last chapter, is described on a cellular level by an action potential. This is the active response of a cell to an external stimulus. It was intensively studied by Hodgkin and Huxley [2], who developed a theoretical description of the cell reaction based on equivalent circuit diagrams. Their work was honoured by the Noble price for medicine in 1963.

Motivated by the Hodgkin Huxley theory, FitzHugh and Nagumo constructed a much more simpler two variable model [3, 29]. For a discussion of the action potential generation, their two coupled equations replace the four equations of Hodgkin and Huxley, which exhibit qualitatively the same physiological behaviour, i.e. they have a similar stability behaviour as the Hodgkin Huxley (HH) equations. Although the FitzHugh Nagumo (FHN) model was originally used to describe neurons, it is a generic prototype for threshold triggered excitable media, which belong to the general class of inhibitor-activator systems. The activator variable is fast, whereas the inhibitor variable is slow. The universal feature of many excitable active systems lies in the structure of their nullclines (see section 3.3 for more details). Quite generally there exists a S-shaped (cubic) and a linear nullcline. The spatially extended form of the FHN equations belongs to the general class of reaction-diffusion systems, which can be used to study self-organised pattern formation far from equilibrium. Due to the coupling of excitation and diffusion, a propagation of waves can arise in these excitable media. For example, it has been seen in spiral wave dynamics [30], the Bhelousov-Zhabotinsky reaction [31] and the morphogenesis of Dictyostelium [32]. The FHN dynamics can also be obtained as mean-field limit of an underlying microscopic chemical reaction model [33], that is based on a birth-death description of the reaction mechanism and a random walk model for the diffusion. Examples of activator-inhibitor systems in quite different areas are given in Table 1.

system	activator	inhibitor
spatial propagation of action potentials in nerves or heart cells	membrane potential	ion conductance
Bhelousov-Zhabotinsky reaction	bromic acid ($HBrO_2$)	ferrous ions (Fe^{2+})
carbon monoxide catalysis on Pt110	carbon monoxide coverage	1×1 surface
spread of epidemics	pathogen	immunity
dynamics of populations	prey	predator
generation of spiral galaxies	gravitation	temperature

Table 1: Examples of activator-inhibitor systems.

3.1   The Hodgkin Huxley model

In the resting state a transmembrane potential V_m can be measured at a cell membrane, due to different ion concentrations on both sides of the membrane.

The different ion concentrations arise, since ion transfer through the membrane is in the passive state only possible for some ion types (e.g. potassium), whereas other ion types can not cross the membrane and are thus accumulated on one side. In this sense the membrane acts as a capacitor and a stationary transmembrane potential according to the Nernst potential can be measured[3]. If the membrane is stimulated externally by applying a current to the membrane, inducing a voltage or mechanically irritating the cell, the properties of the membrane change, resulting in modified ion concentrations and a different transmembrane voltage. Hodgkin and Huxley [2] concluded from their experiments with the giant squid axon, that this response of a cell to an external stimulus can be divided into two classes:

- the sub-threshold linear behaviour and

- the trans-threshold nonlinear behaviour.

The threshold is given by the duration and the strength of the stimulus. An applied current, as stimulus, can be either hyperpolarising, i.e. decreasing the transmembrane potential, or depolarising, i.e. increasing the transmembrane potential. In Figure 4 responses to hyper- and depolarisation of different strengths are shown. It can be seen, that the change of the transmembrane potential according to the resting potential (solid black line) is symmetric to an applied current up to a certain current magnitude (here: $I = 10\mu A$). This is known as the linear, passive response of the cell. For increased stimulus the cell will actively respond by generating an action potential (Figure 5).

Since the membrane acts as an capacitor in the passive state, the linear response can be described by an RC part in an electric circuit. This yields

$$Q = C_m V_m \ , \tag{3.1}$$

with the capacitance C_m. The capacitive current I_{RC} through the membrane can be written as the change of the stored charge per time

$$I_{RC} = \frac{\partial Q}{\partial t} = C_m \frac{\partial V}{\partial t} \ . \tag{3.2}$$

The trans-threshold behaviour is an active response to the stimulus and leads to an action potential. For hyperpolarisation no action potential can be obtained regardless of the size of the stimulus. The nonlinear behaviour of the transmembrane potential is caused by the gating of ion channels. The most important ion types for the generation of an action potential are sodium and potassium. In the resting state the potassium channels are open, whereas the sodium channels are closed. At the beginning of an action potential the potassium channels close and the sodium channels open. This results in an increase of the transmembrane potential due to the flux of positive sodium ions into the cell. If the transmembrane potential reaches a certain value, the voltage-dependent potassium channels open again, whereas the sodium channels close.

---

[3]The stationary transmembrane potential is about the Nernst potential of the potassium ions: $E_K = \frac{RT}{F} \ln \frac{[K]_0}{[K]_i} \simeq V_{\text{rest}} = -62mV$.
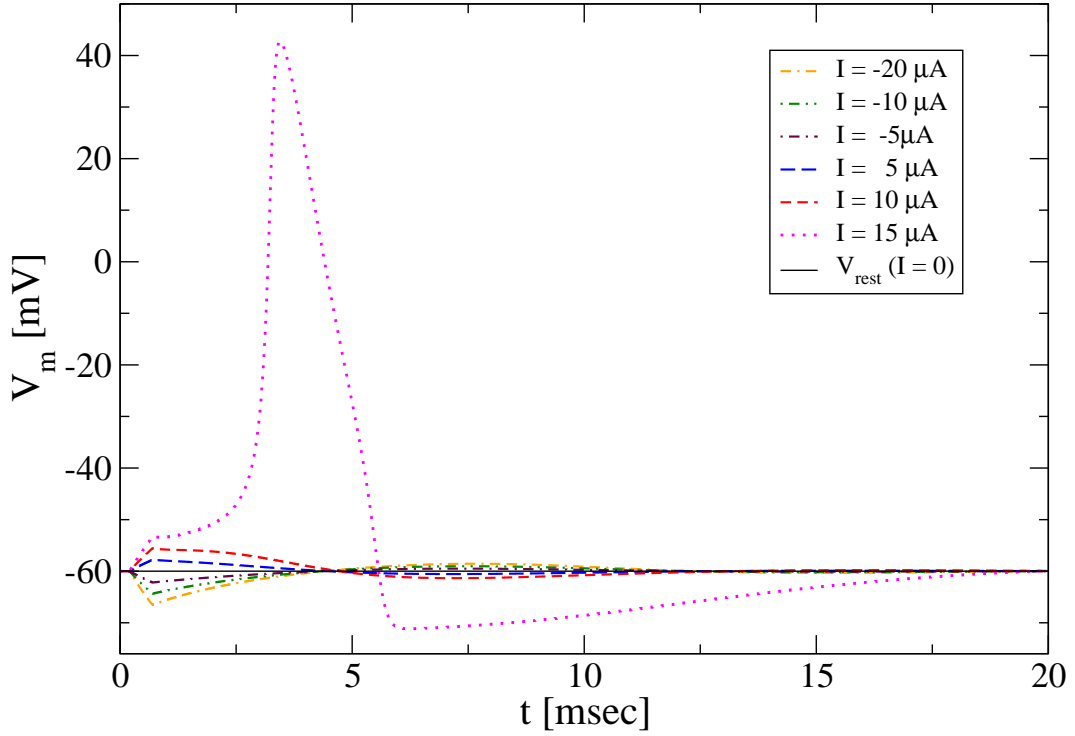
Figure 4: Time evolution of the transmembrane potential after application of different instantaneous current stimuli at t = 0. The different responses of the axon according to the magnitude of the stimulating current can be seen. Up to an applied current of $10\mu A$, the change of the potential is symmetric to hyper- and depolarisation. The time course of the transmembrane voltage after a stimulus of $I = 15\mu A$ is an active response of the cell, the so-called action potential (see also Figure 5).

A flux of potassium ions to the outside of the membrane results, which reduces the transmembrane voltage to its resting state value. The gating of the ion channels is controlled by the transmembrane voltage. The current across the membrane I_α of ion type α depends on the transmembrane potential V_m in relation to the Nernst potential E_α and the conductances g_α of the ion channel, which reads

$$I_\alpha = g_\alpha(V_m - E_\alpha) \ . \tag{3.3}$$

Through extensive voltage clamp experiments Hodgkin and Huxley [2] found a mathematical description of the conductances of the ion channels. The potassium conductance is given by

$$g_K = \bar{g}_K n^4 \ , \tag{3.4}$$

where $\bar{g}_K$ is the maximal conductance of the potassium channel. The gating variable n, corresponds to the fraction of open potassium channels, and the dependence on the fourth power of n in Eq. (3.4) was obtained by Hodgkin and Huxley by fitting the theoretical model to experimental data. The time
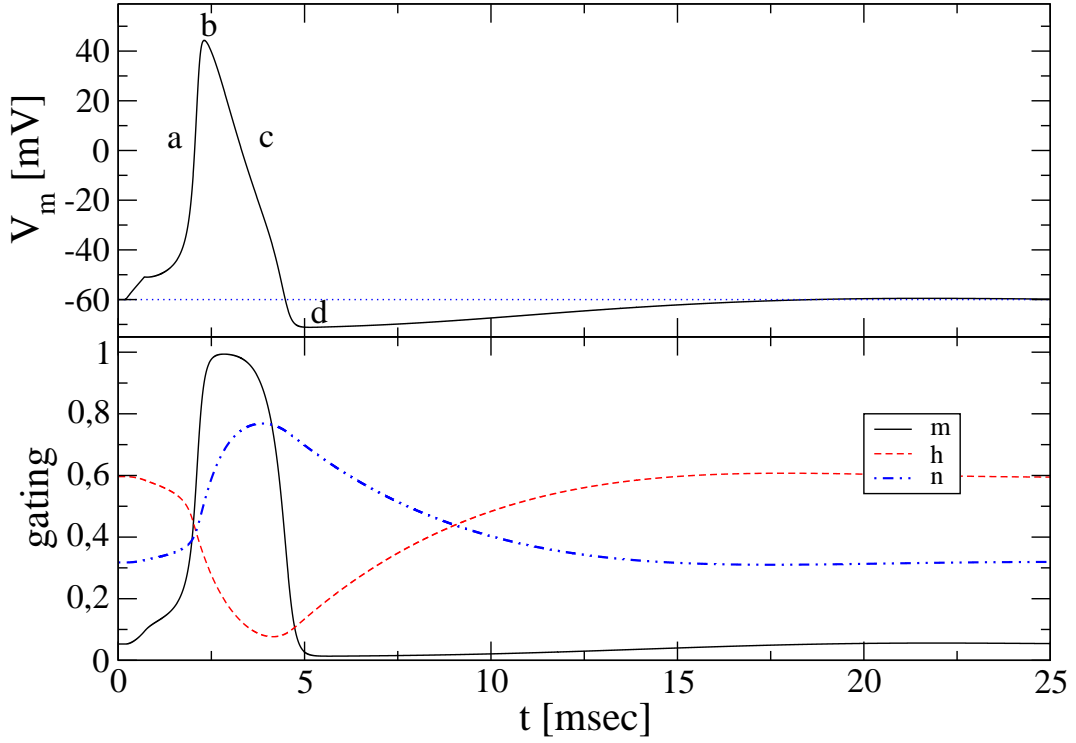
Figure 5: The transmembrane potential (upper part) and the three gating variables n, m and h (lower part) vs. time during an action potential. The dotted line in the upper graph represents the resting state potential. The parts are the depolarisation (rising phase) (a), the peak (b), the repolarisation (decreasing phase) (c) and the hyperpolarisation (d). The return to the resting potential shows the end of the action potential.

evolution of the gating variable n follows a relaxation dynamics

$$\frac{dn}{dt} = \alpha_n(1-n) - \beta_n n \ , \tag{3.5}$$

where α_n and β_n are rate constants for the opening and closing of the potassium channels. Both of these rate constants depend on the transmembrane voltage V_m

$$\alpha_n = \frac{0.01(10 - (V_m - V_{\text{rest}}))}{\exp\left[\frac{10-(V_m-V_{\text{rest}})}{10}\right] - 1} \ ,$$
$$\beta_n = 0.125 \exp\left[-(V_m - V_{\text{rest}})/80\right] \ . \tag{3.6}$$

The resting potential of the cell is described by V_{rest}. The solution of the first order differential equation (3.5) with constant coefficients is

$$n(t) = n_\infty - (n_\infty - n_0) \exp(-t/\tau_n) \ , \tag{3.7}$$

where the relaxation time τ_n from the initial value n_0 to the steady state value

$$n_\infty = \frac{\alpha_n}{\alpha_n + \beta_n} \ , \tag{3.8}$$

14

is given by

$$\tau_n = (\alpha_n + \beta_n)^{-1} \ . \tag{3.9}$$

The conductance of the sodium channels,

$$g_{Na} = \bar{g}_{Na} m^3 h \ , \tag{3.10}$$

depends on the two gating variables m and h. Following a stimulation, the activation parameter m responds by a rapid increase, while the inactivation parameter h decreases slowly. At the resting state, m is zero, corresponding to a situation, where three of four sodium channels are closed (m to the power of three). During an action potential m goes up to one. In contrast to this, h is maximum in the resting state and zero during the action potential. As for the gating variable n of the potassium channels, the time behaviour of m and h is given by first order relaxation kinetics,

$$\begin{aligned}
\frac{dm}{dt} &= \alpha_m(1-m) - \beta_m m = \frac{m_\infty - m}{\tau_\infty^m} \ , \\
\frac{dh}{dt} &= \alpha_h(1-h) - \beta_h h = \frac{h_\infty - h}{\tau_\infty^h} \ ,
\end{aligned} \tag{3.11}$$

but the combination ($g_{Na} = \bar{g}_{Na} m^3 h$) yields a second-order conductance behaviour for the sodium channel. The rate parameters α and β for the gating of the sodium ion channel are [2]

$$\begin{aligned}
\alpha_m &= \frac{0.1\left(25 - (V_m - V_{\text{rest}})\right)}{\exp\left[\frac{25-(V_m-V_{\text{rest}})}{10}\right] - 1} \ , \\
\beta_m &= 4\exp\left[-(V_m - V_{\text{rest}})/18\right] \ , \\
\alpha_h &= 0.07\exp\left[\frac{-(V_m - V_{\text{rest}})}{20}\right] \ , \\
\beta_h &= \left(\exp\left[\frac{30 - (V_m - V_{\text{rest}})}{10}\right] + 1\right)^{-1} \ .
\end{aligned} \tag{3.12}$$

All rate constants α_i and β_i are measured in ms^{-1}. The kinetics of the gating variables and the transmembrane voltage during an action potential can be seen in Figure 5.

The complete response of one cell to a stimulus can be described with the parallel-conductance model [34]. In Figure 6 the equivalent electrical circuit is shown. According to Kirchhoff's first law the sum over all currents must be zero

$$I_K + I_{Na} + I_L + I_{RC} - I_{\text{stim}} = 0 \ . \tag{3.13}$$

Here, $I_K = \bar{g}_K n^4 (V_m - E_K)$ is the potassium current. The sodium current is $I_{Na} = \bar{g}_{Na} m^3 h (V_m - E_{Na})$ and the stimulating current is given by I_{stim}. An additional current $I_L = \bar{g}_L(V_m - E_L)$, the leakage current, was introduced to count for influences of other ions like calcium or chlorine. It is normally small.
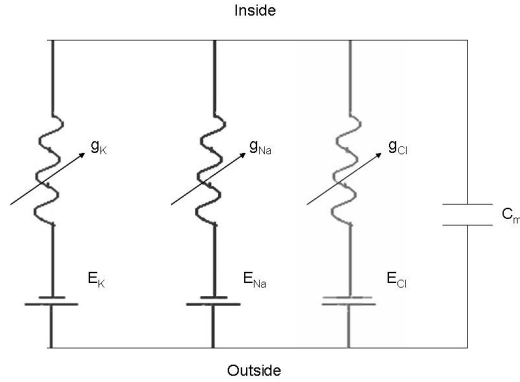
Figure 6: Equivalent electrical circuit diagram of the parallel conductance model. E_i is the Nernst potential and g_i the conductance for the ion type i. C_m represents the capacity of the membrane.

Using I_{RC}, given by equation (3.2), the equations for the four variables of the time dependent Hodgkin Huxley model are written as

$$\frac{\partial V_m}{\partial t} = \frac{1}{C}(I_{\text{stim}} - I_K - I_{Na} - I_L) \,, \tag{3.14}$$

$$\frac{dn}{dt} = \alpha_n(1-n) - \beta_n n \,, \tag{3.15}$$

$$\frac{dm}{dt} = \alpha_m(1-m) - \beta_m m \,, \tag{3.16}$$

$$\frac{dh}{dt} = \alpha_h(1-h) - \beta_h h \,. \tag{3.17}$$

The voltage dependent gating variables n, m and h, which were postulated by Hodgkin and Huxley and derived by fitting the experimental data [2], later turned out to be real structural properties of the ion channels [35, 36]. The parameters of the model are summarised in Table 2.

parameter name	variable range	description
V_m	-80...80 mV	transmembrane voltage
V_{rest}	-60 mV	resting potential
C_m	1.0 mF	Membrane capacitance
$\bar{g}_{Na}$	120.0 mS	maximal sodium conductance
$\bar{g}_K$	36.0 mS	maximal potassium conductance
$\bar{g}_L$	0.3 mS	maximal leakage conductance
E_{Na}	55.0 mV	sodium Nernst potential
E_K	-72 mV	potassium Nernst potential
E_L	-49.387 mV	leakage Nernst potential

Table 2: List of parameters of the Hodgkin-Huxley model and their initial value or parameter range (from [34]).

3.2 Spatial extension of the Hodgkin Huxley model

The induced transmembrane potential of an approximately spherical shaped cell in a stimulating electrical field is the same over the entire cell membrane. During an action potential the excitation of the whole cell can be viewed as synchronous. But considering a long fibre of cells, the excited region is limited and propagation of an activation to regions with cells in their resting state can occur. The aim is to investigate the action potential conduction over a tissue. Therefore one has to extend the Hodgkin-Huxley equations (3.14 - 3.17) to include the ability of a spatial propagation of an action potential. The result are the 'cable equations', which are obtained by applying Kirchhoff's laws to the linear core conductor model [34]. For deriving the cable equations one considers the electrical circuit diagram shown in Figure 7.
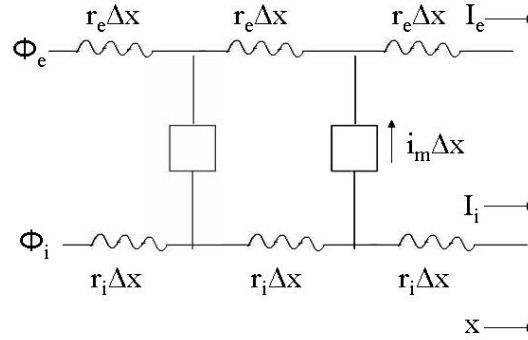
Figure 7: Linear core-conductor model for a single fibre in a restricted extracellular space. I_i and I_e are the longitudinal intracellular and extracellular currents, Φ_i and Φ_e are the intracellular and extracellular potential per unit length and i_m describes the current across the membrane of the cells.

In this approach, extracellular currents I_e are expected to flow only in longitudinal direction along the fibre, whereas the internal current I_i is confined to the axial direction. This is in general true since the fibre radius is many magnitudes smaller than the fibre length. The second assumption is that there exists axial symmetry. The properties of the membrane determine the transmembrane electrical behaviour of the fibre, shown as the open box in Figure 7. In the case of a trans-threshold (or near-threshold) stimulus the behaviour is described by the Hodgkin-Huxley equations and can be represented by the electrical circuit element shown in Figure 6. The representation as a passive RC structure in the linear case (sub-threshold stimulus) is shown in Figure 8. The variations of the internal and external spatial potential $\Phi_{i,e}$ at the membrane per unit length according to Ohm's law are caused by the internal and external currents $I_{i,e}$

$$
\begin{aligned}
\frac{\partial \Phi_i}{\partial x} &= r_i I_i \,, \\
\frac{\partial \Phi_e}{\partial x} &= r_e I_e \,.
\end{aligned}
\tag{3.18}
$$

Figure 8: Electrical representation as an RC element of a cylindrical fibre element of length Δx under linear, sub-threshold conditions.

The external and internal currents I_e, I_i are changed by the transmembrane current i_m

$$\frac{\partial I_i}{\partial x} = -i_m \ ,$$
$$\frac{\partial I_e}{\partial x} = i_m \ . \tag{3.19}$$

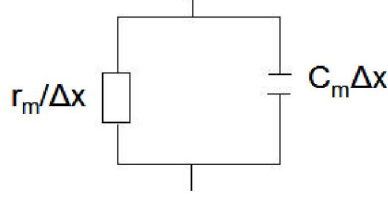These equations fulfil the conservation-of-current principle of Kirchhoff's current law. The membrane current $i_m = \partial V_m / \partial t$ is described by equation (3.14). It is either just the capacitive current in the sub-threshold response or the non-linear ion currents in the trans-threshold case. The transmembrane potential can now be rewritten as $V_m = \Phi_i - \Phi_e$. Using equations (3.18) and (3.19) its second derivative with respect to x reads

$$\frac{\partial^2 V_m}{\partial x^2} = \frac{\partial^2 \Phi_i}{\partial x^2} - \frac{\partial^2 \Phi_e}{\partial x^2} = r_i \frac{\partial I_i}{\partial x} - r_e \frac{\partial I_e}{\partial x} = -(r_i + r_e)i_m \ . \tag{3.20}$$

With

$$i_m = I_K + I_{Na} + I_L + C\frac{\partial V_m}{\partial t} + I_{\text{stim}}$$

and $r_i + r_e = r$, the space- and time-dependent equations of the Hodgkin-Huxley model are

$$\frac{\partial V_m}{\partial t} = \frac{1}{C}\left(\frac{1}{r}\Delta V_m\right) - \frac{1}{C}\sum_{\alpha=1}^{4} I_\alpha(V_m, t) \ , \tag{3.21}$$

$$\frac{\partial n}{\partial t} = \alpha_n(1-n) - \beta_n n \ , \tag{3.22}$$

$$\frac{\partial m}{\partial t} = \alpha_m(1-m) - \beta_m m \ , \tag{3.23}$$

$$\frac{\partial h}{\partial t} = \alpha_h(1-h) - \beta_h h \ . \tag{3.24}$$

In equation (3.21) the sum over the currents is given by

$$I_{\text{tot}} = \sum_{\alpha=1}^{4} I_\alpha(V_m, t) = I_{stim} + \bar{g}_{Na}m^3 h(V_m - E_{Na})$$
$$+ \ \bar{g}_K n^4 (V_m - E_K) + \bar{g}_L(V_m - E_L) \ . \tag{3.25}$$

18

A generalisation to more than one space dimension is straightforward. The equation (3.21) is known as the cable equation.

3.3 The FitzHugh Nagumo model

The FitzHugh Nagumo (FHN) model consists of two coupled non-linear differential equations, which simplified the four differential equations (3.21-3.24) of the Hodgkin Huxley model. The FHN equations show qualitatively the same action potential course as the more realistic HH equations. Furthermore their spatial extensions can be used as description for propagating action potentials. The FHN model was derived from phase space analyses of the HH model by Richard FitzHugh [3, 29].

The analysis of the phase space is a mathematical technique for studying ordinary differential equations (ODEs). Solutions of ODEs describe curves (called paths) in the phase space, whose coordinates are the dependent variables of the system. The state of a physical system is represented by a phase point, which travels along a certain path. Phase space analysis is especially important for ODEs, for which an explicit solution in closed form (an analytical solution) can not be obtained. An overall description of the solutions of these ODEs can be given by exploring special paths (singular points, separatrices and limit cycles), because they determine the topological behaviour of all paths in the phase space. Especially interesting are the so-called nullclines. These are obtained by setting the time derivatives of the variables equal to zero. Accordingly, if the system depends only on two variables, the nullcline of one variable gives the steady state value of this variable as a function of the second variable. By setting both time derivatives zero (this corresponds to finding the intersections of the nullclines), singular, stable and unstable points can be obtained, which describe stable and unstable steady states of the system.

The Hodgkin Huxley model has four independent variables and the corresponding four-dimensional phase space can not be directly visualised. Therefore it is reasonable to study at first the properties of a reduced system by omitting one or two coordinates of the phase space. Since the time constants of the four variables differ by magnitudes, it is suggestive to divide them into two pairs. The transmembrane potential V_m[4] and the gating variable m (where the corresponding relaxation time is τ_m) that vary rapidly, and the gating variables h and n, which vary slowly[5]. Since in a short time the changes of h and n are negligible compared to V_m and m, the behaviour of V_m and m can be studied by setting h and n to a constant resting value and solving the resultant reduced V, m system. The next step is to analyse the effects of changing h and/or n on the behaviour of the reduced system. Then h and n are reintroduced into the system.

In Figure 9 the (V, m) phase space is shown. The m nullcline corresponds to the equation $m_\infty(V_m)$ (Equation (3.8) with n replaced by m), whereas the

---

[4]The time constant is $\tau_V = C_m/g_m$ with $g_m = g_K + g_{Na} + g_L$.

[5]The time constants τ_h, τ_n are about one order of magnitude larger than τ_V and τ_m. Explicit values of the time constants can be found in Tables 1 and 2 in ref. [2].
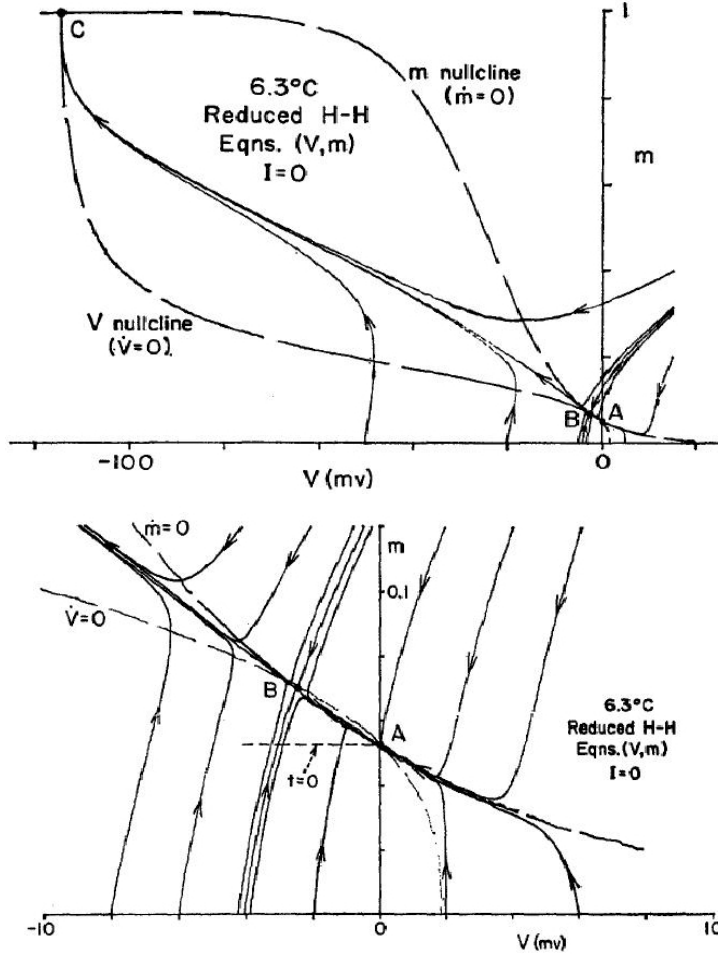
Figure 9: upper graph: (V, m) phase space of the Hodgkin Huxley model. lower graph: Section of the (V, m) phase space to show points A and B in more detail (from [3]).

V_m nullcline gives the steady state value of V_m as a function of m. It can be calculated by setting $dV/dt = 0$ and solving for m

$$m = \left[\frac{I_{\text{stim}} - \bar{g}_K n^4 (V_m - E_k) - \bar{g}_L (V_m - E_L)}{\bar{g}_{Na} h (V_m - E_{Na})} \right]^{1/3} \tag{3.26}$$

As one can see in Figure 9 there are three intersections A, B and C of the two nullclines, which are the singular or equilibrium points. Stability analyses yield, that A and C are stable, while B is a saddle point. The point A corresponds to a stable resting state of the system and C to a stable excited state. One can find two paths leading directly to point B for $t \to +\infty$, which are called threshold separatrices[6]. Along these paths a threshold phenomenon occurs [37]. That means, paths to the right of the separatrices will approach A

---

[6]separatrix = boundary separating two modes of behaviour of the ODE

20
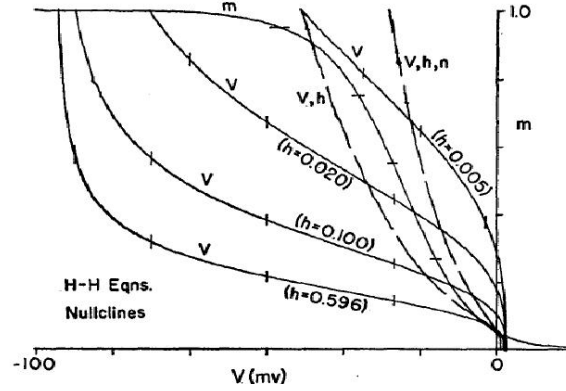
Figure 10: (V, m) phase space diagram for different values of h (from [3]).

and paths to the left will converge to C. The system shows no recovery, since A and C represent stable states. If an instantaneous current pulse is applied or a potential induced, the phase point moves from the resting state A along the line named 't=0' in Figure 9 (lower graph). If the phase point crossed the threshold separatrix, it moves to C. Otherwise it returns to A. Thus the threshold $\Delta V_t = V(A) - V(\text{threshold})$ results in an 'all or non' response of the system.

The influence of changes of n, h or I_{stim} can be studied by equation (3.26). For a fixed V_m, a positive change of I_{stim} or n will increase m. The same is true for a negative change of h. Hence the V_m nullcline raises in response to an increase of I_{stim} or n. The m nullcline is not changed, since it does not depend on n, h or I_{stim}. In Figure 10 both nullclines are shown for different values of h. The points A and B move towards each other, if the V_m nullcline is lowered by increasing h or decreasing I_{stim} or n. This leads to a displacement of the resting potential (point A) to more negative values and a decrease of the threshold magnitude ΔV_t. If the lowering of the nullcline is continued, A and B will coalesce and vanish, if a critical value of n, h or I_{stim} is passed. Accordingly, all solutions will approach C, since it is the only remaining stable point. If the V_m nullcline is raised on the other hand, B and C will move and approach each other until eventually vanishing, so that all solutions will move to A. In this case, the system is not excitable and the resting potential changes to positive values.

Now, let us consider the (V, m, h) phase space. If V_m is displaced by an instantaneous current pulse of size ΔV_t, h equals $h_\infty(0)$. Since V_m is negative, h decreases and the V nullcline raises. Therefore B is moving to the left and taking the threshold separatrices away from the phase point. Consequently the phase point will return to A. If the initial current pulse is greater than the threshold, the phase point starts moving to the left to C. As in the former case, the threshold separatrices moves to more negative potentials. Hence, whether the phase point is overtaken by the separatrices or not, decides, if excitation takes place or not. If the phase point reaches C, it stays in the excited state and no recovery occurs. In the case of the (V, m, h) phase space the threshold
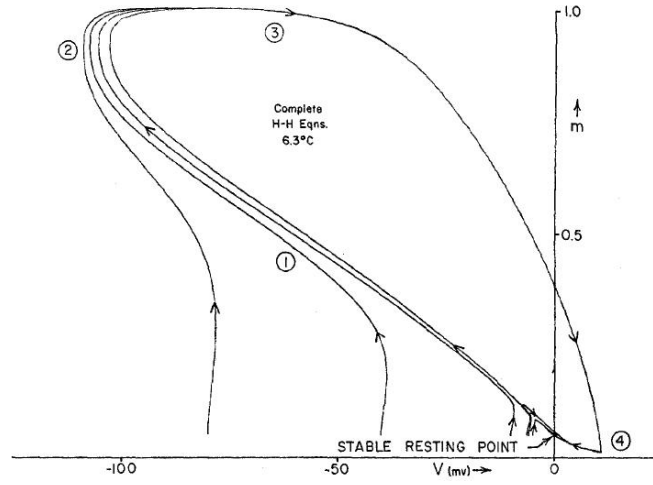
Figure 11: (V, m) phase space diagram for paths after different initial current pulses corresponding to solutions of the complete HH equation. (1) represents the rising phase of the action potential, (2) the peak, (3) the decrease of the potential and (4) the positive after-potential (from [3]).

for a current pulse is increased compared to the (V, m) phase space. Thus h can be characterised as the variable producing accommodation, i.e. increasing the threshold.

If n is reintroduced into the system, the plateau in V_m (the excited state) is no longer stable. This can be understood by the fact, that the V nullcline now raises farther to the left during an action potential and points C and B vanish. Accordingly, the phase point has to return to the resting state at A. Another effect is that point A moves to positive potentials, which leads to a positive after-potential (the hyperpolarisation), when the phase point approaches point A. Since now the membrane potential is positive, $\dot{n}$ and $\dot{h}$ change their sign. Hence n and h return to their resting values and the V nullcline falls again. The singular point A returns slowly to the resting state. The time interval, during which B is absent, describes the absolute refractory period, because no other stable state than the resting state is accessible. The relative refractory period is the time interval, where B returns but is far away from A, and therefore an increased threshold value is obtained. In Figure 11 paths for different initial current pulses are drawn.

Different phenomenological ways for the reduction of the Hodgkin Huxley model to the FitzHugh Nagumo equations exist. As was discussed above, the kinetics of m are very fast compared to that of n and h. With every change of n or h, m can be considered to change instantaneously to its steady state value $m_\infty(V_m)$ at a certain transmembrane voltage. Furthermore, in the given parameter range of the Hodgkin Huxley equations, the sum $n + h$ is constant (approximately 0.8). So the four variable system can be reduced to two equa-

tions with the variables V_m and n:

$$C_m \frac{\partial V_m}{\partial t} = -\bar{g}_{Na} m_\infty^3 (V_m)(0.8 - n)(V_m - E_{Na})$$

$$- \bar{g}_K n^4 (V_m - E_K) - \bar{g}_L (V_m - E_L) + I_{\text{stim}} ,$$

$$\tau_n(V_m) \frac{\partial n}{\partial t} = n_\infty(V_m) - n . \tag{3.27}$$

Due to the fact that the nullcline of V_m is cubic and that of n is linear, the two equations for V_m and n can be converted into the FitzHugh Nagumo equations:

$$\frac{\partial u}{\partial t} = D \frac{\partial^2 u}{\partial x^2} + c(v + u - u^3/3 + z) ,$$

$$\frac{\partial v}{\partial t} = -\frac{1}{c}(u - a + bv) , \tag{3.28}$$

where a, b and c are constants, which control the velocity of excitation, recovery and the threshold for self-excitation, respectively. The variable z represents the stimulus. The diffusive term $D \partial^2 u / \partial x^2$ is introduced in analogy to the space- and time-dependent Hodgkin Huxley model, where D prescribes the diffusion coefficient. A constant for the time evolution of u is defined by $1/c$. On the other hand c/b defines a time constant for the time evolution of v. Thus, for numerical calculations a maximal time step size is determined by

$$\Delta t = \frac{1}{10} \min(\frac{1}{c}, \frac{c}{b}) .$$

A relationship between time and space is given by the diffusion coefficient $D = \Delta x^2 / \Delta t$. Thus a condition for the maximal spacing $\Delta x = \sqrt{D \Delta t}$ is obtained. In all calculations time steps and spacings are applied, which obey these conditions and represent a continuum description.

A physiological interpretation of u and v is given by R. FitzHugh in [29], i.e. u is roughly associated with the membrane voltage and v is the so-called recovery variable, corresponding to the gating variables h and n. To understand this one can look again at the phase space of the Hodgkin Huxley model. As was described before, the HH model is split into two subsystems (V, m) and (n, h). The pair (V, m) corresponds to u and represents excitability. The variable v is commensurate to the pair (h, n), which represents accommodation and refractoriness. To set up a simplified model with retained physiological properties, one can eliminate one dimension from each subsystem by linear projection. The variables n and $(-h)$ can be replaced by their average $v = 0.5(n - h)$, since their curves have similar shapes during an action potential. From a geometrical viewpoint, the path of an action potential in the (n, h) plane can be fitted by the line $n + h = 0.85$. Consequently this line is considered as a v axis and points of the (n, h) plane are projected onto lines with constant $v = 0.5(n - h)$. In the same way, with $u = V - 36m$, points of the (V, m) plane are projected onto lines of constant u. The lines of constant u are nearly parallel to the threshold separatrices of the (V, m) system. Hence the char-
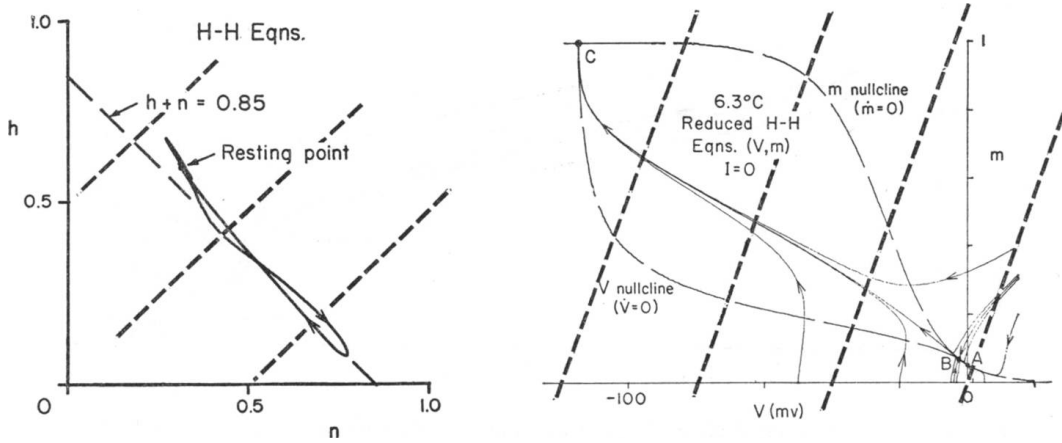
Figure 12: (n, h) phase space diagram (left graph) and (V, m) phase diagram (right graph) to illustrate the projection lines and the simplification method to yield u, v coordinates (from [3]).

acteristic threshold phenomenon[7] is preserved. In Figure 12 the projections and paths during an action potential are shown. Results obtained from the Hodgkin Huxley equations (3.21- 3.24) and the FitzHugh Nagumo equations (3.28) can be compared by solving the HH equations and then calculating u_{HH} and v_{HH} from:

$$
\begin{aligned}
u_{\text{HH}} &= V - 36m \, , \\
v_{\text{HH}} &= 0.5(n - h) \, .
\end{aligned}
\tag{3.29}
$$

Then the behaviour of u_{HH} and v_{HH} can be compared with that of u_{FH} and v_{FH}, which were calculated according to equations (3.28). This is shown in Figure 13. Three stimuli of the same size were applied at $t = 0, 8$ and 24. In both models two action potentials are obtained. The sign of the activation variable of the FitzHugh Nagumo model is changed in comparison to u_{HH}. Given that it only depends on the definition of the transmembrane potential, i.e. if the transmembrane potential is defined as $\Phi_e - \Phi_i$ or with the opposite sign, this is no important difference. The diverse parts of an action potential are obtained in both models for u_{HH} and $-u_{\text{FH}}$, including the rising phase, the peak, the decrease, the hyperpolarisation and finally the recovery to the resting value. Both figures show just two action potentials although three stimuli were applied. The small peak of the activation variable in the left figures at $t = 8$ is a vestige of the second stimuli. In this case the applied current was not large enough to yield a second action potential, because the cells were still in their relative refractory period. Accordingly both models include the property of refractoriness in an analogous way. The differences in the shape of the activation and inactivation variable of the FHN model compared with the HH equations are not important for investigating the main features of the

---

[7]The threshold phenomenon is represented by the divergence of paths when approaching the point B.
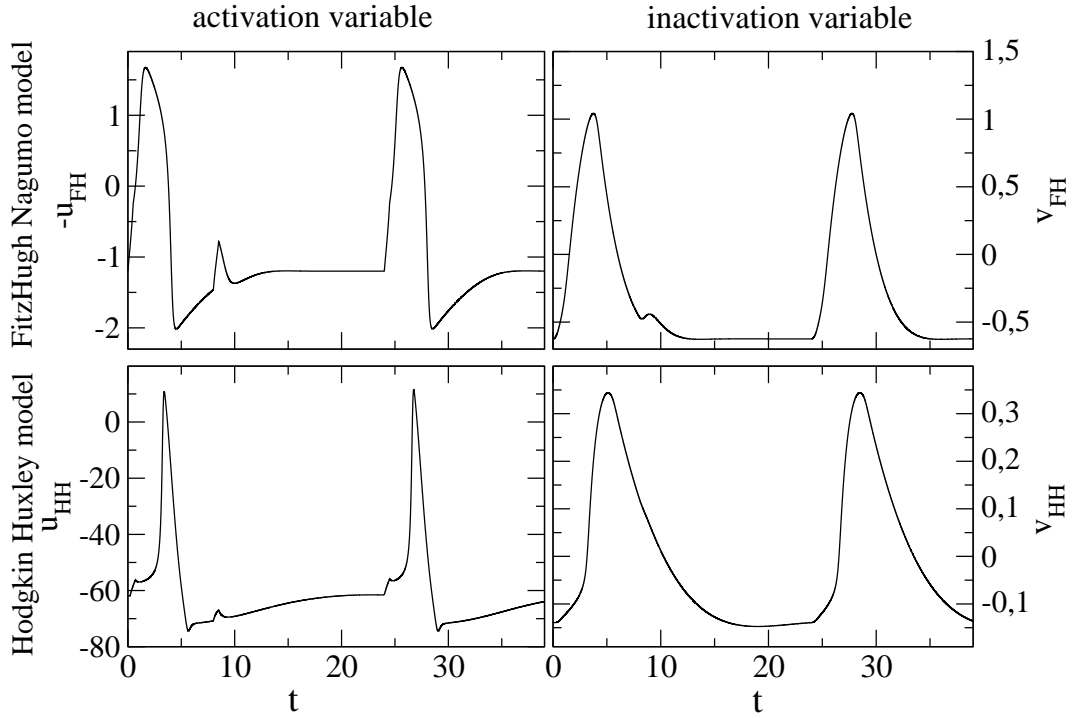
24

Figure 13: Comparison of the FitzHugh Nagumo equations (3.28) with the Hodgkin Huxley equations (3.21-3.24). The variables u_{FH} and v_{FH} are the activation and inactivation variables of the FitzHugh Nagumo equations and u_{HH}, v_{HH} were calculated from V_m, m, n and h from the Hodgkin Huxley equations by Equation (3.29).

models like threshold behaviour and refractoriness. They play an important role, when comparing simulated action potentials with measured ones from different cell types, where the shape is the discriminating property. Hence, if the qualitative behaviour of action potentials and their propagation is studied, the FitzHugh Nagumo model can be applied as a reduced version of the Hodgkin Huxley model.

In addition, the comparison between results calculated from the Hodgkin Huxley equations and the FitzHugh Nagumo equations (Figure 13) gives an impression of the ranges of the variables u_{FH} and v_{FH}. The resting transmembrane potential of $V_m \approx -62$ mV is represented by $u_{FH} = 1.2$ for $v_{FH} = -0.6$. The peak value of the transmembrane voltage during an action potential is $V_m \approx 40$ mV, whereas u_{FH} is approximately -1.6 at maximum. Thus the range of the activation variable u_{FH} of $[1.5, -1.3]$ reflects the range of the transmembrane voltage of $[-80, 40]$ mV. The range of the inactivation variable of $[-0.7, 1.2]$ corresponds to the the range of the gating variables n and h of $[0, 1]$.

3.4 Analytical reduction of the Hodgkin Huxley model

To determine the properties and physiological ranges of the three coefficients a, b and c of the FitzHugh Nagumo equations (3.28):

$$
\begin{aligned}
\frac{\partial u}{\partial t} &= D\frac{\partial^2 u}{\partial x^2} + c(v + u - u^3/3 + z) \ , \\
\frac{\partial v}{\partial t} &= -\frac{1}{c}(u - a + bv) \ ,
\end{aligned}
$$

an analytical transformation of the HH equations to the FHN equations is sought. Abbott and Kepler [38] proposed a procedure to reduce the four dynamical variables (V_m, m, n, h) to two (u, v). It consists of two steps:

- Replacing the gating variable m for the activation of the sodium channels by its asymptotic value $m_\infty(V_m)$

- Introducing an auxiliary potential variable U and replacing h and n by their asymptotic values $h_\infty(U)$ and $n_\infty(U)$

The first step can be done, because the time scale associated with m is much smaller than that of h or n (see chapter 3.3), i.e. one gives up some accuracy of the model over very short time scales. By neglecting the differential equation (3.23) for m, the reduced Hodgkin-Huxley system reads:

$$
\begin{aligned}
C\frac{\partial V_m}{\partial t} &= -\tilde{I}_{\text{tot}}(V_m, m_\infty(V_m), n, h) \ , \\
\frac{dn}{dt} &= \alpha_n(1 - n) - \beta_n n \ , \\
\frac{dh}{dt} &= \alpha_h(1 - h) - \beta_h h \ , \quad\quad (3.30)
\end{aligned}
$$

where

$$
\tilde{I}_{\text{tot}} = \bar{g}_K n^4(V_m - E_K) + \bar{g}_{Na}(m_\infty(V_m))^3 h(V_m - E_{Na}) + \bar{g}_L(V_m - E_L) \ .
$$

A simple replacement of h and n by their asymptotic values $h_\infty(V_m)$ and $n_\infty(V_m)$ would destroy the ability of the model to generate action potentials, since it would equalise the time scales of m, n and h. Consequently, the action potential would be terminated by n and h as quickly as m could initiate it.

To account for the retarded reaction of n and h to a variation of the membrane voltage V_m, one can introduce an auxiliary potential variable U. With this potential U, n and h can be replaced by their asymptotic values $n_\infty(U)$ and $h_\infty(U)$. The replacing of the gating variables by their asymptotic values is possible, because in the Hodgkin-Huxley model the gating variables depend only on V_m and do not directly influence each other. The resulting equations are

$$
\begin{aligned}
C\frac{\partial V_m}{\partial t} &= -\tilde{i}_{\text{tot}}(V_m, m_\infty(V_m), n_\infty(U), h_\infty(U)) \ , \\
\frac{dU}{dt} &= g(V_m, U) \ , \quad\quad (3.31)
\end{aligned}
$$

with

$$\begin{aligned}
\tilde{i}_{\text{tot}} &= \bar{g}_K n_\infty^4(U)(V_m - E_K) + \bar{g}_L(V_m - E_L) \\
&+ \bar{g}_{Na} m_\infty^3(V_m) h_\infty(U)(V_m - E_{Na}) \, .
\end{aligned} \tag{3.32}$$

The time dependence of U can be obtained by equating the time derivative of I_{tot} at constant V_m in Equation (3.25) and $\tilde{i}_{\text{tot}}$ in the reduced form (3.32)

$$\frac{\partial I_{\text{tot}}}{\partial h} \frac{dh(V_m)}{dt} + \frac{\partial I_{\text{tot}}}{\partial n} \frac{dn(V_m)}{dt} = \left(\frac{\partial \tilde{i}_{\text{tot}}}{\partial h_\infty} \frac{dh_\infty(U)}{dU} + \frac{\partial \tilde{i}_{\text{tot}}}{\partial n_\infty} \frac{dn_\infty(U)}{dU} \right) \frac{dU}{dt} \, . \tag{3.33}$$

Equation (3.33) ensures, that the implicit time dependence of $\tilde{i}_{\text{tot}}(U(t))$ mimics the time dependence of I_{tot} in the full Hodgkin-Huxley model through changes of the variables h and n, whereas V_m and m are constant.

The time evolution of n is obtained by inserting Equations (3.9) and (3.8) into Equation (3.5):

$$\frac{dn}{dt} = \frac{n_\infty(\Phi) - n(t)}{\tau_n(\Phi)} \, . \tag{3.34}$$

$n_\infty(\Phi)$ is the asymptotic value of n for a certain potential Φ, which can be given by V_m or U. Replacing now n by its asymptotic value for U yields:

$$\frac{dn}{dt} \approx \frac{n_\infty(V_m) - n_\infty(U)}{\tau_n(V_m)} \, . \tag{3.35}$$

The equivalent equation for h is:

$$\frac{dh}{dt} \approx \frac{h_\infty(V_m) - h_\infty(U)}{\tau_h(V_m)} \, . \tag{3.36}$$

Inserting (3.35) and (3.36) into Equation (3.33) yields the conditional equation for $g(V_m, U)$:

$$g(V_m, U) = \frac{dU}{dt} = \frac{A}{B} \, , \tag{3.37}$$

with

$$A = \left[\frac{\partial I_{\text{tot}}}{\partial h} \left(\frac{h_\infty(V_m) - h_\infty(U)}{\tau_h(V_m)} \right) + \frac{\partial I_{\text{tot}}}{\partial n} \left(\frac{n_\infty(V_m) - n_\infty(U)}{\tau_n(V_m)} \right) \right] \bigg|_{\substack{h = h_\infty(U) \\ n = n_\infty(U)}} \tag{3.38}$$

and

$$B = \frac{\partial \tilde{i}_{\text{tot}}}{\partial h_\infty} \frac{dh_\infty(U)}{dU} + \frac{\partial \tilde{i}_{\text{tot}}}{\partial n_\infty} \frac{dn_\infty(U)}{dU} \, . \tag{3.39}$$

The functions $h_\infty(\Phi), n_\infty(\Phi), m_\infty(\Phi), \tau_n(\Phi)$ and $\tau_h(\Phi)$ with the potential $\Phi = V_m$ or U are obtained by inserting Equation (3.6) into (3.9) and (3.8) as well

as Equation (3.12) into (3.11)

$$h_\infty(\Phi) = \frac{0.07\exp(-\Phi/20)}{0.07\exp(-\Phi/20) + 1/\left[\exp\left(30-\Phi\right)/10\right)+1\right]} \; ,$$

$$n_\infty(\Phi) = \frac{0.01(10-\Phi)/\left[\exp\left((10-\Phi)/10\right)-1\right]}{0.01(10-\Phi)/\left[\exp\left((10-\Phi)/10\right)-1\right] + 0.125\exp(-\Phi/80)} \; ,$$

$$m_\infty(\Phi) = \frac{0.01(25-\Phi)/\left[\exp\left((25-\Phi)/10\right)-1\right]}{0.01(25-\Phi)/\left[\exp\left((25-\Phi)/10\right)-1\right] + 4\exp(-\Phi/18)} \; ,$$

$$\tau_h(\Phi) = \frac{1}{0.07\exp(-\Phi/20) + 1/\left[\exp\left((30-\Phi)/10\right)+1\right]} \; ,$$

$$\tau_n(\Phi) = \frac{1}{0.01(10-\Phi)/\left[\exp\left((10-\Phi)/10\right)-1\right] + 0.125\exp(-\Phi/80)} \; .$$

To identify the parameters a, b and c of the FitzHugh Nagumo equations (3.28), one has to compare these equations with the reduced Hodgkin-Huxley equations (3.31). Therefore one has to solve the conditional equations for $\tilde{i}_{\text{tot}}(V_m, U)$ and $g(V_m, U)$ with the nonlinear function $h_\infty(\Phi), n_\infty(\Phi), m_\infty(\Phi), \tau_n(\Phi)$ and $\tau_h(\Phi)$. As a consequence no simple relationship between the parameters of the Hodgkin-Huxley model and the parameters a, b and c of the FHN equations exists.

Another way to determine the effect of the parameters a, b and c is to study numerical solutions of the time dependent FHN equations without spatial degrees of freedom. These solutions are shown in Figure 14. Each diagram shows the solutions for the variation of one parameter, whereas the other parameters are kept constant at the standard values: $a = 0.7$, $b = 0.8$, $c = 3.5$ with time steps $\Delta t = 0.01$. To determine, which parameter defines the refractory period and the excitation threshold, two stimuli were applied: one at $t = 0$ and the second at $t = 9$. The small peak, seen at about $t = 9$ in most cases, represents a passive response of the cell as described in chapter 3.1, i.e. the second stimulus is applied during the refractory period and can thus not activate an action potential. R. FitzHugh [29] proposed a physiological meaningful range for the parameters:

$$b \in (0, 1); \;\; a \in (1 - \frac{2}{3}b, 1); \;\; b < c^2 \; .$$

In Figure 14 I the influence of different values of parameter b on the time evolution of u is shown. If a is set equal to 0.7, one can extract from the physiological parameter range given by R. FitzHugh a lowest value of $b = 0.45$ (green dash-dotted line) and an upper value $b = 0.99$ (black solid line). The red dashed line ($b = 0.8$) shows, for comparison, the result for u with the standard parameters mentioned above. Decreasing of b yields a second action potential, but its shape is changed in comparison to the first one. This demonstrates that the refractory period is not yet completed, but the threshold for excitation was overcome. Additionally the stability of the resting state is reduced, which is indicated by the oscillation around the resting potential. In summary, decreasing b leads to a decrease of the threshold for excitation and
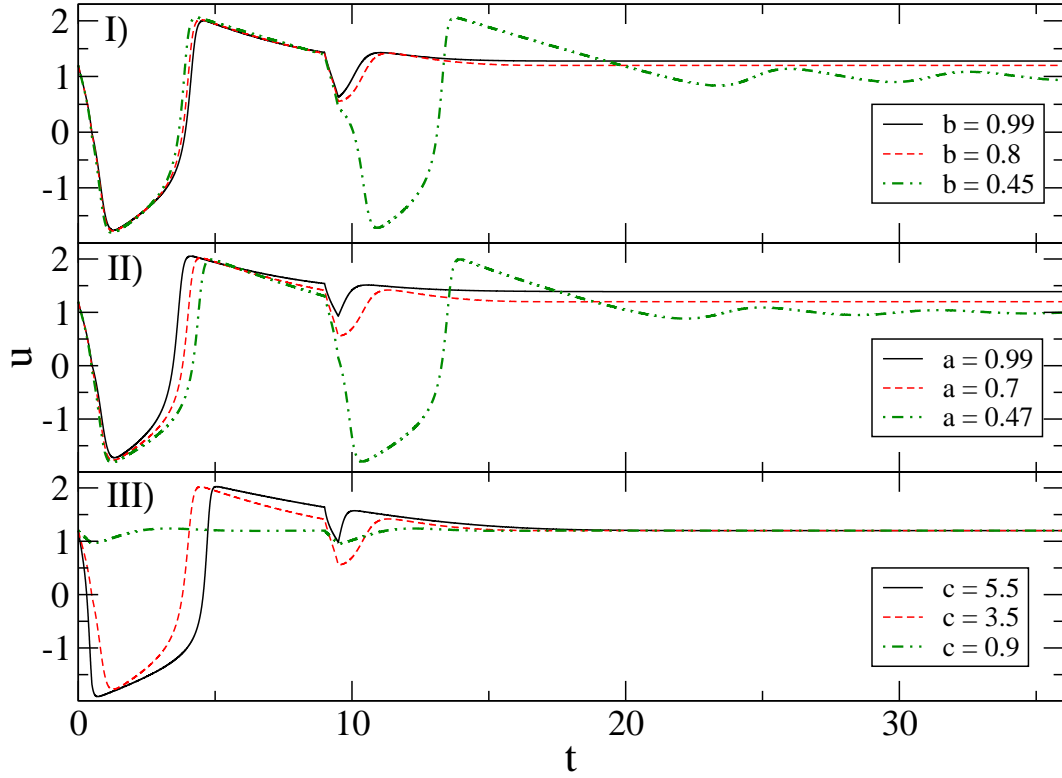
Figure 14: Numerical solutions for u in dependence of time t after application of two stimuli at $t = 0$ and $t = 9$ for the FHN model. The parameters are: $a = 0.7$, $b = 0.8$, $c = 3.5$ and time steps $\Delta t = 0.01$. Decreasing of b leads to a reduced excitation threshold and a reduced stability of the resting state (I). The variation of a (II) changes the duration of the refractory period. Parameter c does not influence the refractory period, but the strength of the cell response to a stimulus (III).

the stability of the resting state.

The effect of variations of the parameter a are shown in Figure 14 II. The value $a = 0.47$ (green dash-dotted line) is the lower boundary value for $b = 0.8$ and $a = 0.99$ corresponds to the upper boundary. $a = 0.7$ was chosen as the standard value for a. It can be seen that the decrease of a below a critical value (here: $a = 0.6$) leads to a second action potential as in the case of variation of the b parameter in Figure 14 I. In the present case, however, the shape of the second action potential is similar to that of the first one, which indicates that the refractory period is almost finished. Additionally, the shape of the action potential is changed for different values of a, i.e. the increase is stronger and the second decrease is slower for increased a. Consequently, a decrease of the parameter a in the FHN model shortens the length of the refractory period. The potential oscillates around the resting state for smaller a, but this effect is not as strong as for reduced values of b. This shows, that the parameters a and b mainly determine the refractory period and the stability of the resting state, respectively. However, both parameters also influence the corresponding other property.
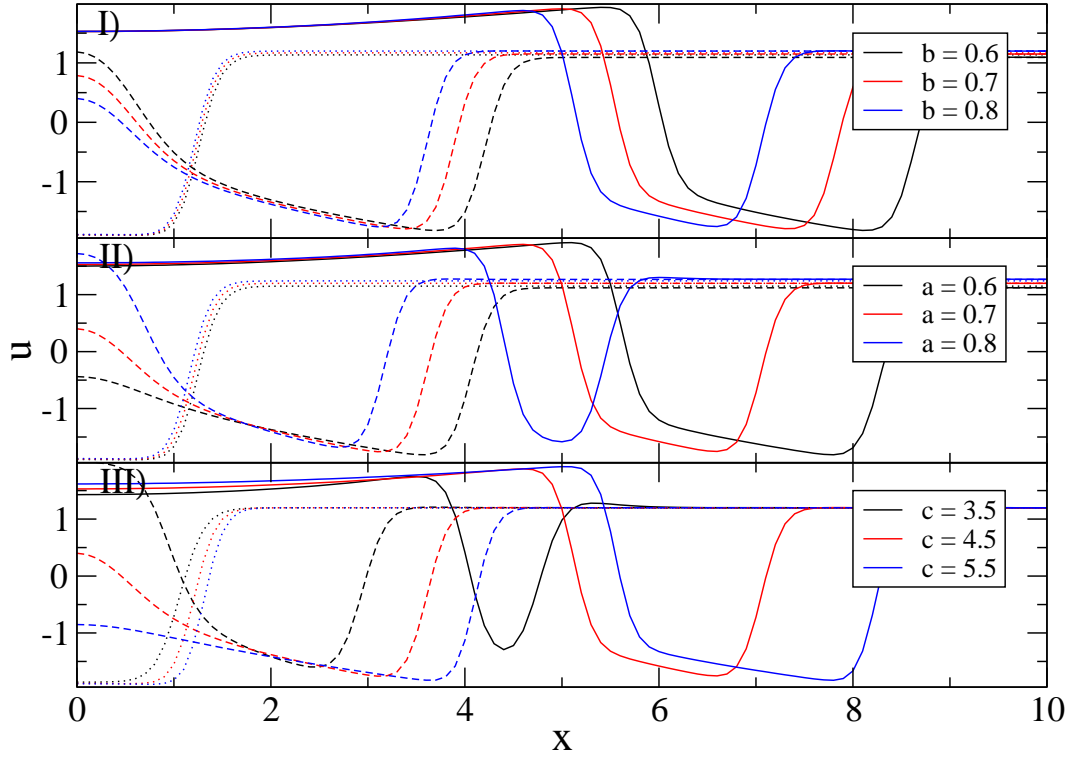
Figure 15: Numerical solutions for u in dependence of x after application of one stimulus at $t = 0$ for the spatio-temporal FHN model (3.28) in one dimension. The parameters are $a = 0.7$, $b = 0.8$, $c = 5.5$ and $D = 0.1$ with timesteps $\Delta t = 0.01$ and grid size $\Delta x = 0.1$. The dotted lines correspond to solutions at time $t = 2$, the dashed lines at $t = 6$, and solid lines at $t = 12$. A decrease of a or b, and an increase of c yield an increased conduction velocity. For $a \geq 0.9$ and $c \leq 3.5$ no propagation occurs.

Figure 14 III shows the results for different c values. The minimal value of c in the physiological range is given by $\sqrt{b} = \sqrt{0.8} \approx 0.9$ (green dash-dotted line). No upper boundary exists for parameter c. For all values of c the second stimulus can not excite a second action potential. This shows that the refractory period is not influenced by c. But an increase of c results in a higher magnitude, a stronger decline at the beginning and an increased duration of the action potential. For strongly decreased c (here: $c = 0.9$) even the first impulse can not excite an action potential. These changes reveal that c changes the ability of the cell to respond to a stimulus and the strength of this response.

Atrial fibrillation is described by spatio-temporal patterns of the membrane voltage. Hence the FitzHugh Nagumo model has to be analysed according to spatial and temporal degrees of freedom. The conduction velocity of an excitation wave in the spatio-temporal FHN model is mainly determined by the diffusion coefficient D characterising the spreading of the voltage. But additionally it is influenced by the parameters a, b, and c, because they change cell properties like the excitation threshold, the refractory period and the ability to respond to a stimulus. These influences are studied in numerical simulations of

30

the spatio-temporal FHN model in one dimension (Figure 15). The standard parameters of the simulations are $a = 0.7$, $b = 0.8$, $c = 5.5$, $D = 0.1$ with time steps $\Delta t = 0.01$ and grid size $\Delta x = 0.1$. An increased value of c compared to the time dependent case is used, since for smaller values of c propagation of the excitation will fail due to the influences of the diffusion.

In Figure 15 II solutions of Equations (3.28) are shown for different values of the parameter a. A decrease of a leads to an increase of the conduction velocity of the excitation wave. If a exceeds a certain value (here $a \geq 0.9$), the excitation wave becomes unstable and conduction is suppressed after a certain distance. For the parameter b (Figure 15 I) this effect is absent, but a decrease of b results in an increase of the wave speed as well. The behaviour is inverted for the parameter c (Figure 15 III): an increase of c triggers an increase of the speed of the travelling wave. If c is reduced below a critical value ($c \leq 3.5$), the wave becomes unstable and the propagation of the wave front is stopped.

4 Simple scenarios for atrial fibrillation mechanisms

After this study of the main properties of the FitzHugh Nagumo model, an overview of scenarios, discussed in the literature, to investigate the generating mechanism of AF is given in this chapter. In the early twentieth century first attempts have been made to theoretically describe atrial fibrillation. Since this time, many studies were performed to investigate the mechanisms of AF. Three main theories have been established (see section 2.2 for a description). The underlying concept of two of them is reentry and among these essentially three different mechanisms of reentry were proposed. They are schematically sketched in Figure 16.
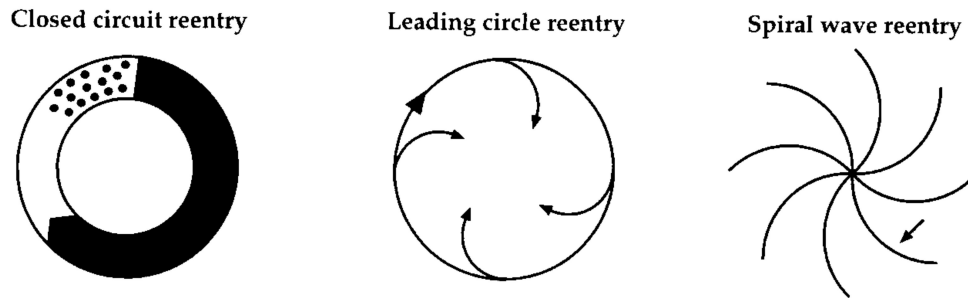

Figure 16: Different kinds of reentry discussed in the literature (from [13]).

In 1913 Mines [39] proposed that the reentry occurs in closed circuits. This requires that the core of the reentry circuit is inexcitable. In anatomical tissue this can be caused by obstacles like the pulmonary veins or the venae cavae, by regions of inexcitability caused by cicatrices or heart diseases, and by the arrangement of potential conducting pathways. Since the circuit is closed, the time for one circulation, the circuit time, is given by the path length divided by the conduction velocity. Closed circuit reentry can only occur, if the circuit time is greater than the refractory period of the substrate. In AF the substrate seems to be more functional than fixed [40], but the closed circuit reentry can not account for the dynamic nature of reentry in arrhythmias. To improve the circuit theory, Allessie *et al.* [41] introduced the leading circle concept in 1977 as a first detailed conceptual model of functional reentry. In this concept a leading circle establishes itself at the smallest circuit size, which can be continuously active. The product of conduction velocity and refractory period prescribes the wavelength[8] and defines the minimum circuit size for reentry. In this case the circuit time and consequently the fibrillation rate depend solely on the refractory period. An important difference to the closed circuit concept is that the core of the leading circle is continuously excited by invading centripetal impulses from the circulating reentrant wave.
A more generalised concept of continuous activity in excitable media, the spiral wave concept, was put forward by Pertsov *et al.* [43]. In this concept the core is fully excitable, but not excited. From a kinematic theory of spiral

---

[8]This was defined by Mines [39] and later quantified by Wiener and Rosenblueth [42].

waves, proposed by Mikhailov and Zykov [44], it is known that the stability of spiral waves depends strongly on the curvature of the wavefront. The key concept behind is the source-sink relationship of the propagating activation wave. The wavefront can propagate as long as unexcited but excitable cells, the so called 'sink', are activated by the diffusive current from the source, i.e. the depolarised cells at the wavefront. Thus there exists a relationship between the source current and the amount of tissue being excited by the source current. In Figure 17 this relationship is schematically shown for different curvatures of the wavefront. For a concave curvature the sink decreases with the ongoing propagation up to the point, that no excitable tissue is reachable and the propagation fails. A planar wavefront diffuses straightforward with a constant conduction velocity. The velocity is increased for a concave curvature, because a smaller sink is attached to the source compared to the case of the planar wave. This results in a larger current from the activated cells to the excitable tissue and thus a faster activation of the sink. A decreased velocity is obtained for a convex wavefront, where a larger sink is connected to the source. Propagation may fail in this case, if the source current available for excitation is reduced too much to yield an activation. The necessary condition for a circulation is the appearance of a velocity gradient along the wavefront. Hence, the convex curvature has to increase from the outside to the inside of the spiral wave along the activation wavefront. A limitation of the spiral wave
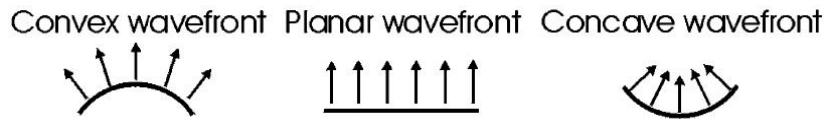

Figure 17: Explanation of different stabilities of propagating waves in dependence on the curvature of their wavefront. In the case of a concave wavefront the sink is reduced by the propagation leading to the failing of this propagation. If the wavefront is convex, the propagation can fail as well, if the sink is too large in relation to the source.

approach is the difficulty to predict the stability and the rate of reentry based on simple electrophysiological properties as conduction velocity and refractory period.

In experiments indirect evidences were found that support all three kinds of reentry. One prediction of the leading circle concept is, for example, that the number of waves accommodated in the atria should be related to the wavelength. Indeed it was found by Rensma [45], that the ability to induce AF in dog hearts is related to the wavelength under various conditions. In addition, the rate of functional reentry seems to be related to the refractory period as predicted by the leading circle concept [46]. On the other hand, only spiral waves could be directly visualised[9] in high-density mapping studies [47, 48, 49]. Up to now it is under discussion, which of the reentry mechanisms is most reliable. The great limitation of the leading circle concept is the missing account

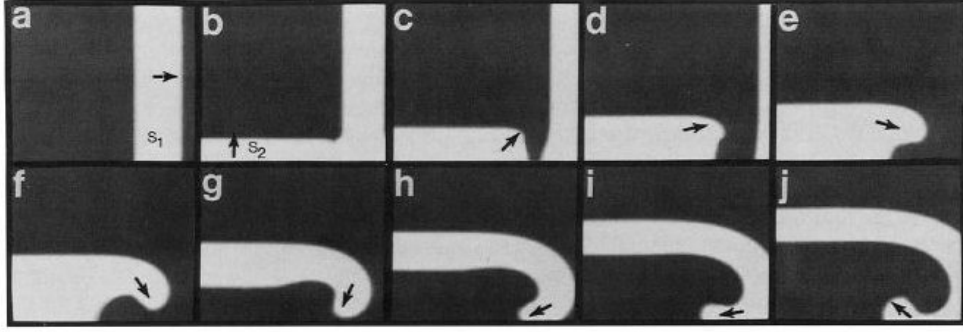[9]The visualisation is carried out with voltage sensitive dyes.

Figure 18: Video frames showing the generation of a spiral wave by crossfield stimulation in a homogeneous and isotropic array. (a) Basic planar wave propagates from left to the right. (b)-(j) Time course of a second generated wave front. The pictures show the activation pattern at the following intermediate steps. (b) Premature planar wave is initiated perpendicularly from the bottom to the border of the array. (c) The second wave, initiated in (b), breaks into the refractory tail of the first one and develops a pronounced curvature. (d)-(j) The wave front curls and a clockwise rotating spiral is initiated (from [43]).

for key biophysiological properties like electrotonic interaction[10] or complex properties of the medium and dynamic core behaviours. The predictions of the spiral wave concept seem to correspond more closely to the results of clinical and experimental observations [50]. Hence, it is currently the favoured mechanism of reentry.

In numerical studies [43] and in experiments [51] the generation of spiral waves is often performed by crossfield stimulation (see Figure 18). A planar wave is initiated and a second premature planar wave, perpendicular to the first, is excited with some delay. The second wave front can break into the refractory tail of the first one and develop a pronounced curvature, which can lead to a curling of the wavefront and thus a rotating spiral. Extensive studies of the properties of spiral waves in dependence of the ratio of recovery to excitation rate and in dependence on the excitation threshold have been performed by Winfree [52].

Many experimental observations [51, 53, 54] show that spiral waves can be anchored and stabilised by anatomical obstacles. This was investigated by numerical simulations [55, 56, 57] of spiral waves on a two-dimensional circular area with a circular hole inside and no-flux boundary conditions[11] (see Figure 19). In these simulations the spiral wave is stabilised by the obstacle and its properties depend on the size of this obstacle. From an anatomical viewpoint the obstacle represents inexcitable tissue. In section 5.3 the generation of spiral waves by obstacles, corresponding to functionally modified tissue, is studied in detail based on the FitzHugh Nagumo equations.

---

[10]The current flow between neighbouring cells, which changes the local action potential morphology.

[11]$du/dn = 0$. u is the potential. n is the unit vector perpendicular to the boundary.
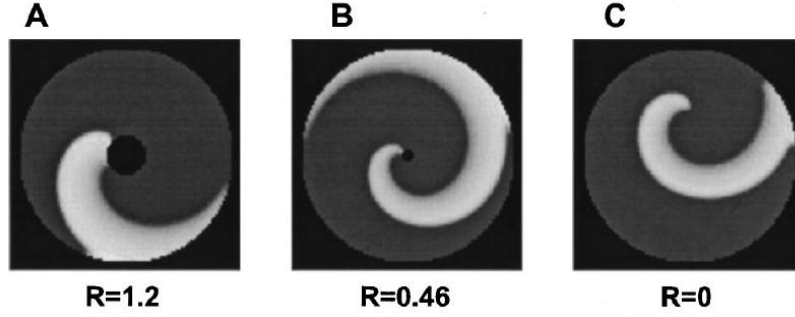
Figure 19: Reentry in an annulus with various values for the inner radius R_i and a fixed outer radius $R_o = 5.2$ cm. Snapshots of activity for A) $R_i = 1.2$ cm, B) $R_i = 0.46$ cm, and C) $R_i = 0.0$ cm, no hole (from [56]).

Over a long time the multiple wavelet theory by Moe *et al.* (see section 2.2) was the favoured theory to explain AF, since atrial fibrillation is a chaotic process with irregular spatio-temporal patterns of the voltage. The multiple wavelets were associated with multiple reentry circuits or spiral wave breakups and the fibrillatory pattern should result from the primary arrhythmia mechanism. In the last years, studies [19, 27, 26, 58] show that the fibrillatory pattern is not caused by the generating mechanism itself. The irregularity has rather two different origins. On the one hand it can be caused by the spatially variable properties of the atrial tissue leading to perturbations and changes of conducted waves. This effect is known as 'fibrillatory conduction'. On the other hand, it might be caused by the interference of different wavefronts, e.g. waves generated by a single source (ectopic focus or spiral wave) and periodic and regular wavefronts emanating from the sinus node. In numerical simulations [59, 60] fibrillatory conduction is studied by spatial variations of acetylcholine, which is the cause of an additional potassium current. The spatial patterns can lead to spiral wave breaks and these are visible as irregular patterns in the simulated electrocardiogram.

In this work the focus is on the second proposed mechanism: the interaction of a stable reentrant source and the activation waves generated by the sinus node. The results are presented in the following chapter.

5 Irregular wave patterns caused by physiologically modified regions

The emergence of irregular wave patterns due to the disturbance of initially regular waves by physiologically modified regions is studied in this chapter. The first step is the investigation of mechanisms and configurations, which can yield an ectopic focus (section 5.2) or a spiral wave (section 5.3). Thereby, the cell properties like excitability and refractoriness are modified in local regions by spatial variations of the parameters b and c of the FitzHugh Nagumo model (3.28). The analyses focus on the generating mechanisms of these irregularities, the conditions and limits for their occurrence, and their properties and influence on the characteristics of an overall fibrillatory state. With these results, the interference of regular planar excitation waves with the irregular wave patterns is investigated in a two-dimensional model including both atria. Spatial variations of the fibrillation rate and the generation of certain spatio-temporal patterns are analysed and presented in section 5.4. At the beginning of this chapter, the methodology of the calculations is explained, including the modelling of physiologically modified regions, which we shortly call 'obstacles' in the following. Also, the method of solving the FitzHugh Nagumo equations and the analyses of the solutions are discussed in section 5.1.

5.1 Methodology

The basis of this work is the numerical calculation of the FitzHugh Nagumo equations

$$
\begin{aligned}
\frac{\partial u}{\partial t} &= D\left(\frac{\partial^2 u}{\partial x^2} + \frac{\partial^2 u}{\partial y^2}\right) + c(v + u - u^3/3 + z)\,, \\
\frac{\partial v}{\partial t} &= -\frac{1}{c}(u - a + bv)\,.
\end{aligned}
\tag{5.1}
$$

The wave patterns observed in the atria are approximated as two-dimensional, because the activation waves propagate mainly on the surface of the atrial tissue due to its small thickness (in contrast to the ventricular tissue). For simplicity, the calculations are carried out on a two-dimensional square simulation area. This simulation area can be considered to represent an isolated section of atrial heart tissue as used in experiments [53, 61, 62]. In this respect, the calculations neglect the complex geometry of the atria.

Physiologically modified regions, i.e. the obstacles, are modelled by a circular variation of parameter b or c around a centre (x_0, y_0) according to

$$
\begin{aligned}
b(x,y) &= b_0 - (b_0 - b_{\text{red}})\exp(-\sqrt{(x-x_0)^2 + (y-y_0)^2}/\xi_b)\,, &(5.2) \\
c(x,y) &= c_0 - (c_0 - c_{\text{red}})\exp(-\sqrt{(x-x_0)^2 + (y-y_0)^2}/\xi_c)\,, &(5.3)
\end{aligned}
$$

where $c_0 = 5.5$ and $b_0 = 0.6$ represent the standard values of the calculation, corresponding to healthy tissue. The parameters c_{red} and b_{red} are the reduced
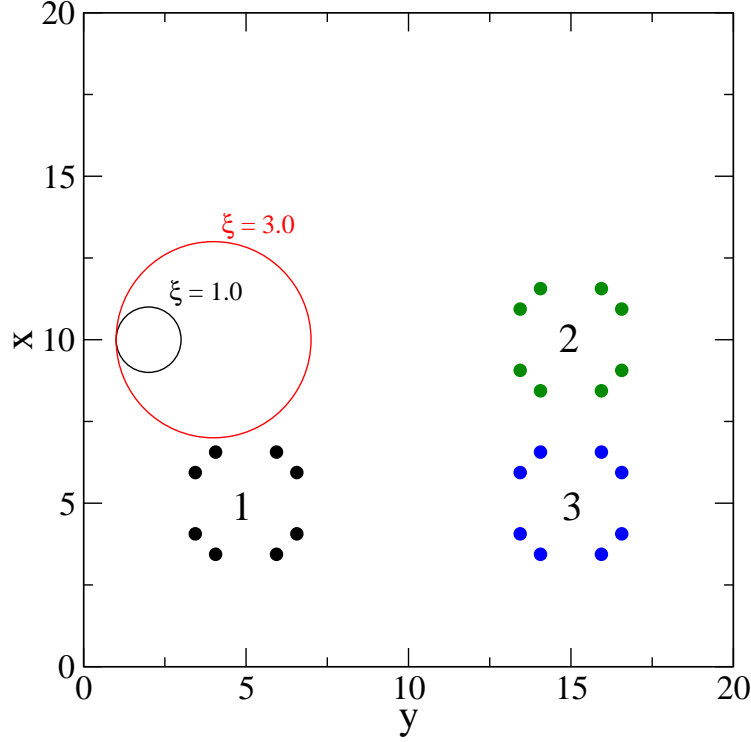
Figure 20: Schematic representation of the simulation area. The circles labelled with ξ show different sizes of obstacles. The dots of the circles marked with '1', '2' and '3' represent observation sites for the frequency analysis (see section 5.1.1).

values of parameter b and c, which represent the physiologically modified properties. The correlation length ξ defines the distance, where the parameters b and c have increased to a value of $b_0 - (b_0 - b_{\text{red}})/e$ and $c_0 - (c_0 - c_{\text{red}})/e$, respectively. In the following ξ is called the obstacle size. The standard parameters of the calculations are $a = 0.7$ and $D = 0.1$. A schematic representation of the simulation area with two representative obstacles of different size is shown in Figure 20. As initial condition the whole simulation area represents cells in the excitable resting state. Thus the activation variable u and the inactivation variable v are set to the resting state values of $u = -1.2$ and $v = 0.6$. The boundary conditions of the simulation area are of von Neumann type, i.e. $\partial u / \partial n = 0$ with $\vec{n}$ as the unit vector perpendicular to the boundary. Note that v is a scalar variable associated with each space point without coupling to neighbouring ones. Physically, the von Neumann boundary conditions mean that no flux of u is present over the boundary. If u were conserved, it would be reflected at the boundary. However, u is not a conserved quantity, due to the reaction term $du/dt = c(v + u - u^3/3 + z)$ in eq. (3.28), which creates sources[12] and sinks for u. Moreover, since the activation wavefront of the FHN model is followed by a refractory tail, it can not excite backwards and is thus not reflected. Numerical calculations of the spatial FHN model reveal, that

---

[12]A source is, for example, an applied current z.

these boundary conditions describe the experimental configuration in the most faithful way.

The two nonlinear coupled partial differential equations (PDEs) are solved with the MATLAB$^{©}$ software. The calculation is based on the finite element method (FEM). In this method the simulation area is split into a union of simple geometric objects (here: triangles). The triangles form a mesh and each vertex is called a node. The solution $w(x, t)$ of the PDE is expressed in terms of a series of basis functions $\Phi(x)$,

$$w(x, t) = \sum_{i=0}^{n} U_i(t) \Phi_i(x) \ . \tag{5.4}$$

A suitable basis are 'tent' or 'hat' functions, which are linear at the triangles and take the value 0 at all nodes x_j except of x_i. The coefficients $U_i(t)$ are the values of the solution at the nodes.

For the explicit solution, the differential equations are transformed into a system of algebraic equations by a method called 'the variational method' in the finite element approach. In this method the differential equations are multiplied with the basis function $\Phi(x)$ and integrated over the triangular mesh. The task is then to minimise the integral.

Inserting the basis set decomposition of $w(x, t)$ into the variational equation yields the set of equations to solve. A detailed description of the FEM can be found in [63, 64]. Important for the accuracy and correctness of the solutions is the size of the grid. It has to be optimised, so that the change of the variables between two nodes is smaller than an appropriate tolerance ε. Therefore, the 20×20 simulation area is decomposed into 4225 node points and 8192 triangles. The nonlinearity $u^3(\vec{x}, t)$ in the FHN equations (3.28) is treated as an inhomogeneity, which is independent of the solution $u(\vec{x}, t_i)$ at the actual time step t_i. This inhomogeneity can be approximated by the solution $u(\vec{x}, t_{i-1})$ of the last time step. We finally obtain

$$e \frac{\partial \vec{w}(\vec{x}, t_i)}{\partial t} - \frac{\partial}{\partial \vec{x}} \left(f \frac{\partial \vec{w}(\vec{x}, t_i)}{\partial \vec{x}} \right) + g \, \vec{w}(\vec{x}, t_i) = h \ , \tag{5.5}$$

with $\vec{w} = (u, v)^T$ and

$$e = \begin{bmatrix} 1 \\ 1 \end{bmatrix}, \ f = \begin{bmatrix} D \\ 0 \end{bmatrix}, \ g = \begin{bmatrix} -c & \frac{1}{c} \\ -c & \frac{b}{c} \end{bmatrix}, \ h = \begin{bmatrix} -\frac{1}{3}(u(\vec{x}, t_{i-1}))^3 \\ \frac{a}{c} \end{bmatrix} \ . \tag{5.6}$$

This approximation is always possible, if the time step Δt is chosen small enough, since then u varies only very little within Δt.

The time-dependent solutions $u(x, y, t)$ and $v(x, y, t)$ can be visualised by three-dimensional graphs and their evolution as a movie of these graphs. But these movies require a manual inspection. For an automatic analysis one can detect the phase singularities of the solutions and investigate the frequency distribution within the simulation area. Both techniques are explained in the following section.

5.1.1 Methods for analysing the activation patterns

The detection of the phase singularity provides an automatic analysis of spiral waves by the lifetime of the phase singularity and their time evolution. Thus one can automatically classify the solutions of the numerical calculations according to the following aspects: (i) generation of a spiral wave, (ii) temporal stability of spiral waves, and (iii) motion of the spiral waves. A schematic graph of a spiral wave is shown in Figure 21. Additionally, one can see the
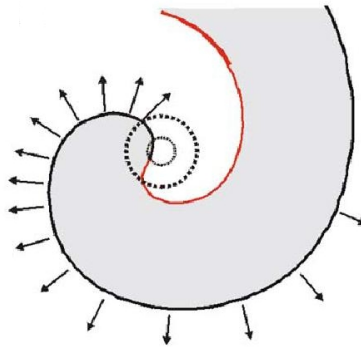

Figure 21: Schematic graph of a spiral wave (from [50]). The solid black line marks the activation wavefront, which propagates in direction of the arrows. The repolarisation front is represented by the red solid line. The thin dotted line represents the pathway of the tip of the spiral, the phase singularity.

propagation directions of the activation and repolarisation wavefront. Generally the activation generated by the spiral wave propagates from the inside of the spiral (thick dashed line in Figure 21) to the outside of the excitable medium. In the simplest case the shape of the spiral wave is constant and it rotates with constant angular velocity around a circle of constant size. But it can also move around in various ways, e.g. by meandering.

The phase singularity is the point of coincidence of the convex curved activation front (black line), which starts at the inner part of the spiral and propagates to the outside, and the repolarisation front (red line), which follows the activation front. The phase singularity corresponds to a non-excited point at the inner tip of the wavefront with an uncertain phase, because all phases of activity meet there. Its time evolution is shown in Figure 21 by the thin dotted line. The definition of the phase singularity is based on phase space analysis. The phase angle is defined as the angle of the coordinates of the phase space variables (e.g. $V(t), V(t - \tau)$) around the phase space origin for all time values at this point. It lies in the range of $-\pi$ and π. One can create a phase map by assigning the phase angle to each point of the spatial grid at a certain time. The phase singularity describes in this sense a point, where the phase is uncertain, whereas the neighbouring sites show a continuous progression of phase around the phase singularity. The mathematical definition of the phase singularity is given by:

$$n = \oint_C \vec{ds}\vec{\nabla}\Phi \; , \tag{5.7}$$

where n is the topological charge, $\Phi(r)$ the local phase and C a closed curve. If n equals $\pm 2\pi$, the area enclosed by C includes a phase singularity.

Different methods [60, 65, 66] have been proposed for the automatic detection of phase singularities. In this work a variation of the detection algorithm, proposed by Zou *et al.* [60] and based on a combination of Bray's method [65] with an image-analysis method, is used. The flow diagram of the detection algorithm is shown in Figure 22.
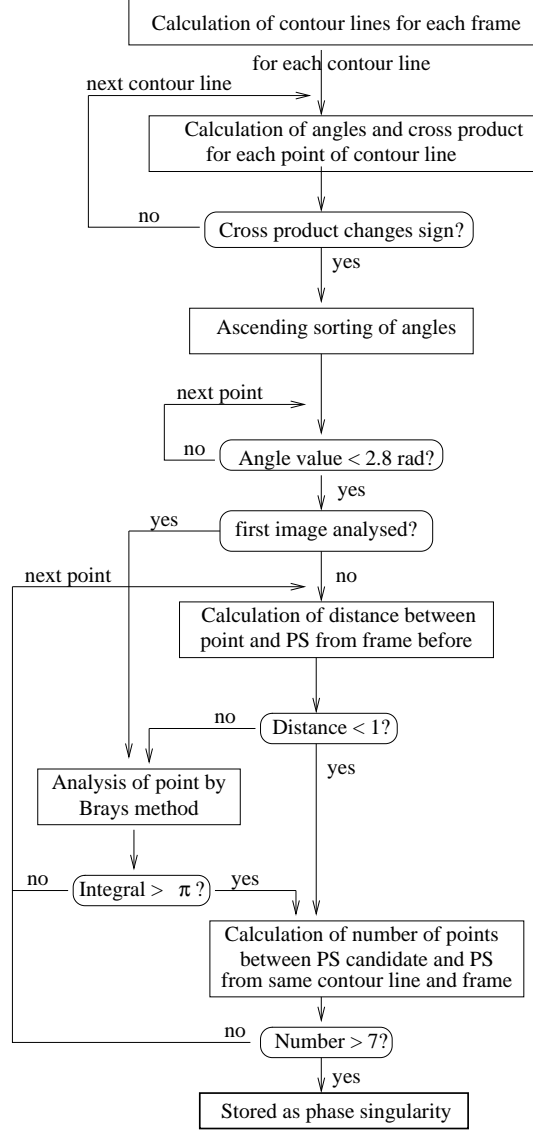

Figure 22: Schematic graph of algorithm for detection of phase singularities.

The location of phase singularity candidates by Bray's method is based on the calculation of n using equation (5.7). The first step is to determine the two phase space variables. In experiments only one variable is measured, the voltage V. The corresponding variable in the FHN model is the activation variable u. The second variable of the phase space $u(x, y, t + \tau)$ is recreated

from $u(x,y,t)$ by the time-delay τ. It is important, that the two variables are linearly independent. To fulfil this condition, τ has to be chosen in such a way, that paths in the phase space $(u(x,y,t), u(x,y,t+\tau))$ describe closed curves. Thus τ should be approximately the duration of the increase of the action potential. If τ is chosen too large, the paths in the phase space cross. The phase space is constructed by calculation of the phase angle:

$$\Theta(x,y,t) = \arctan\left(\frac{u(x,y,t+\tau) - \overline{u}(x,y)}{u(x,y,t) - \overline{u}(x,y)}\right) . \qquad (5.8)$$

In earlier works, the value of $\overline{u}(x,y)$ was taken as the mean of $u(x,y,t)$ over all time records at the point (x,y). In this work $\overline{u}(x,y) = 0.04$ is chosen from the phase space as a point surrounded by all trajectories. This guarantees that the phase is well-defined in the range $[0, 2\pi]$. The line integral eq. (5.7) at a point (x,y) is calculated by the following steps:

(i) evaluation of $\nabla\Phi$ as the difference of Φ between two points,

(ii) choice of a set of points lying on a circle of a certain diameter around the investigated point,

(iii) summation over the difference of $\nabla\Phi$ between two adjacent points on the circle multiplied with the distance between the points.

The radius for the circle is set to 0.5. Hence, points closer than 0.5 to the boundary can not be analysed by this method. Points, for which the integral yields values larger than π, are defined as a phase singularity. Due to numerical errors and the chosen algorithm the value of 2π is practically not obtained here for a phase singularity.

The idea of the image-analysis method is to find the points, at which the curvature of the wavefront changes from convex to concave, i.e. the point between the activation and the repolarisation front. Therefore, first contour lines of the activation waves are constructed. The threshold for the contour line is set to $u = -0.8$. With this value one obtains two contour lines for every excitation waves, since u reaches the threshold value twice, at the rise and the decrease of u. To analyse the curvature of the contour line, the angles between a point and its adjacent neighbours are calculated as shown in Figure 23. To minimise local noise effects due to the sampling of the contour line, one consecutively constructs lines between pairs of points at a certain distance r (see Figure 23), and calculates the angle between these lines. Here, r is set to 1. The time of the analysis is minimised by checking, if the contour line exhibits a change of curvature from convex to concave. Otherwise it does not contain a phase singularity. This is done by calculation of the cross product of the lines of a point to its neighbours. If the contour line changes its curvature, the cross product should change the sign at a certain point. Hence, only contour lines, where the cross product exhibits this change of sign, are analysed further. Phase singularities correspond to the points with the minimal angle. Hence, the next step is an ascending sorting of the angles according to their values and eliminating
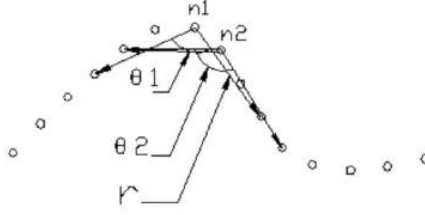
Figure 23: Illustration for the calculation of the angles between the points of the contour line (from [60]).

of angles from the further analysis, whose values are above a certain threshold. The threshold is set to 2.8 radians. To assure that no detection errors occur for the first phase singularity candidates, the integral (5.7) is calculated for these first candidates by Bray's method as described before. If it is larger than π, the point is classified as a phase singularity. If already phase singularities were detected in frames before, it is tested, if the phase singularity candidates are the consecutive places of the formerly detected phase singularities or if they are new phase singularities. Therefore the potential phase singularity candidates are judged by the 'last frame rule' [60]. That means, the smallest distance between the phase singularity candidate and the phase singularities, detected in the frame before, is computed. If the distance is larger than a threshold value (here: 1 space unit), the point is analysed by Bray's method in order to determine, whether it is a new phase singularity or a detection error.

If the distance is smaller than the threshold value or the phase singularity candidate is defined as phase singularity by Bray's method, the last step of the detection algorithm is an analysis by the so-called interval rule. This rule prevents false positive detection of points very close to each other to be identified as distinct phase singularities. Therefore the number of points is computed, which are lying between this point and previously detected phase singularities in the same frame and contour line. If this number is larger than a certain value (here: 7), then the point is conclusively classified as a phase singularity. Otherwise it is eliminated. The various steps in the analysis are repeated for all points on a contour line and for all contour lines in one frame. To reduce the computation time, but still obtain a consecutive detection of one phase singularity, the analysis is performed every ten timesteps.

The second analysis deals with the frequency distribution caused by the disturbance of the excitation wave by the obstacle. Therefore $u(x, y, t)$ is recorded at special sites of the simulation area as schematically shown in Figure 20. These recordings are analysed by a detection routine of the action potential. Only peaks after a simulation time $t > 10$ (corresponding to 1000 time steps) are used for further analysis to assure that the activation pattern has already stabilised. The inverse of the mean over the time intervals between consecutive peaks determines the frequency at the investigated point. Subsequently, the local frequencies are averaged over the different observation sites. In this

way one obtains a spatial distribution of the frequency of excitation and an average frequency of the whole spiral. This provides valuable insights into the properties of the activation pattern, as e.g. the fibrillation rate and typical spatial patterns of the excitation.

5.2 Ectopic activity

In this section the possibility to obtain ectopic foci with the FHN model and their properties are investigated. Ectopic foci are regions in the atria distinct from the sinus node, which generate activation waves. In optical mapping studies and spatial resolved ECG recordings, they are often localised in the regions of the pulmonary veins. Ectopic foci are assumed to be hyperactive cells, which are self-excitatory, i.e. the transmembrane potential raises without external stimulation until the threshold value is reached and an action potential results. In Figure 24 the time evolution of the transmembrane potential of a hyperactive cell is shown.
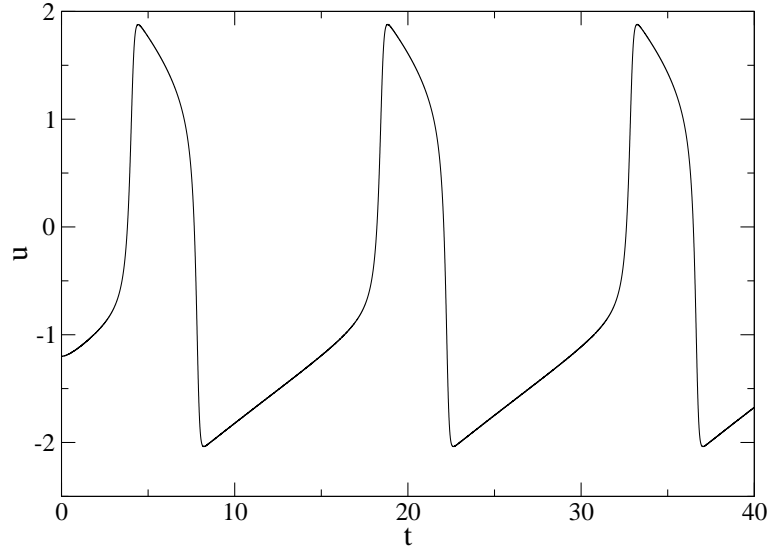

Figure 24: Time evolution of u for a region of ectopic activity. The resting state is not stable and u raises until the threshold value is crossed, resulting in an action potential.

To model a tissue with changed properties resulting in ectopic activity, the resting state stability b is spatially varied according to Equation (5.2). To analyse the conditions necessary for ectopic activity, a manual inspection of the solutions $u(x, y, t)$ and a frequency analysis as described in section 5.1.1 is performed. The results of these analyses yield a dynamical phase diagram of the ectopic activity in dependence on the characteristic size ξ_b of the hyperactive tissue and the difference in the stability of the resting state $\Delta b = b_0 - b_{\text{red}}$ (see Figure 25). As can be seen in the diagram, different time evolutions of u are obtained. Large sizes of hyperactive tissue result in an ectopic activity as described before, i.e. the modified tissue is self-excitatory and generates
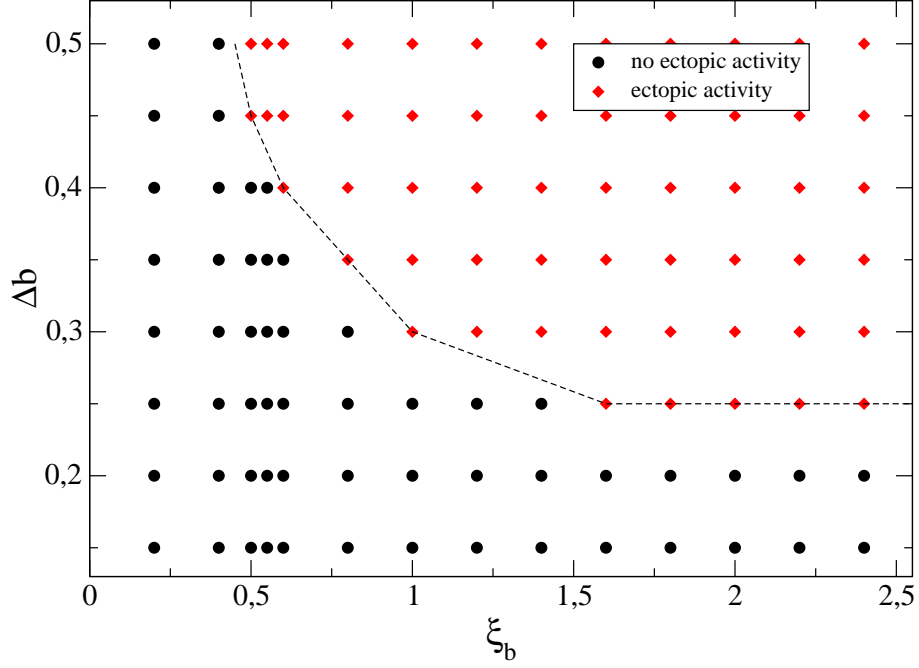
Figure 25: Ectopic activity in dependence on ξ_b and Δb. The dotted line marks the region of ectopic activity. No ectopic foci can be observed below $\Delta b \approx 0.25$ and for sizes of hyperactive tissue smaller than $\xi_b \approx 0.4$.

activation waves, which propagate radially. Thus it acts as a pacemaker. If ξ_b is decreased below a critical value ($\xi_b \approx 0.5$ for $\Delta b \approx 0.45$), the ectopic activity vanishes and only small oscillations of the activation variable u are found. These oscillations around the resting state value are observed in the modified region, where the stability b is reduced. The oscillations reflect the instability of this patch of tissue. An activation is not attained due to the strong diffusive current from the modified tissue to the surrounding. If ξ_b is decreased further, the system is kept in the resting state as long as there is no external stimulation. A constant value of $u = 1.2$ is then obtained in the whole simulation area.

If the difference of excitability Δb is reduced for a constant size of hyperactive tissue, the transition from ectopic activity to a stable resting state in the whole system is observed as well. A minimal $\Delta b \approx 0.25$ is required to obtain ectopic activity. The results of the frequency analysis are shown in Figure 26. If ξ_b is increased for a certain value of Δb, the frequency of the ectopic activity increases until a saturation occurs. The saturation value of the frequency is mainly determined by the refractory period of the tissue. The refractory period in turn depends on the strength and speed of the cell reaction, which are influenced by changes of parameter b. Larger values of b yield a slower reaction and a smaller strength and thus a longer refractory period. Hence, the saturation frequency is decreased with decreasing Δb.
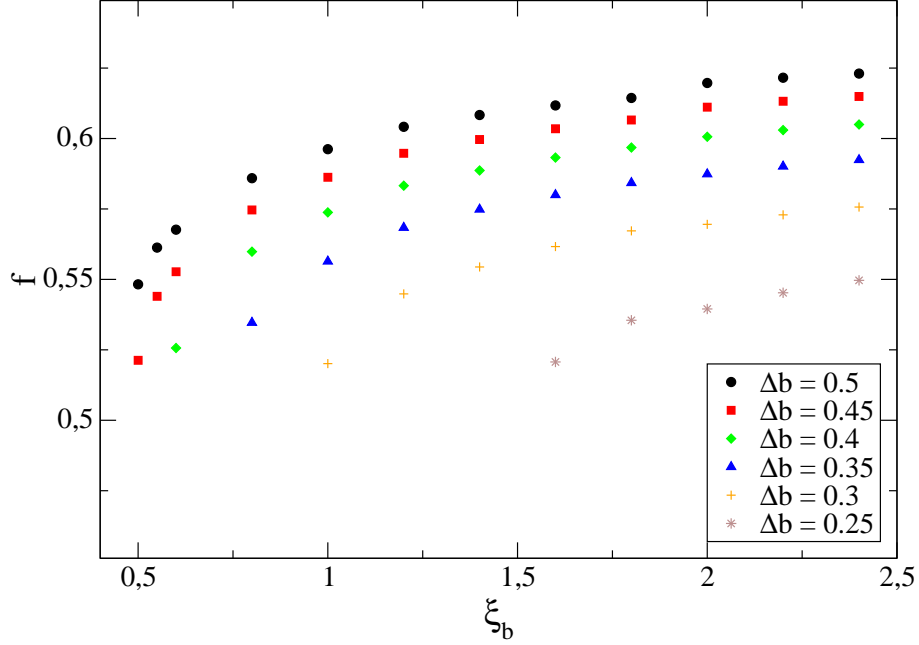
Figure 26: Frequency of ectopic activity in dependence of the size ξ_b of hyperactive tissue for different values of Δb. With increasing ξ_b the frequency increases and eventually saturates, since the frequency of ectopic activity is determined by the refractory period of the tissue. Decreasing Δb at fixed ξ_b yields a decrease of the frequency.

5.3 Spiral waves

Now the possibility to generate spiral waves by 'anchoring' of planar excitation waves to obstacles is studied, as well as the influence of the obstacle properties on the characteristic properties of the waves. The obstacles, e.g. the pulmonary veins themselves, the venae cavae themselves, or some localised region of modified tissue, influence the propagation of an incident wave. The obstacle tissue is considered to be not fully excitable. They are modelled as cells with a reduced excitability by spatial variation of parameter c according to Equation (5.3). Thereby, $b = 0.6$, $a = 0.7$ and $D = 0.1$.

Two different configurations are investigated. First the obstacle is located near the boundary, which may be realised in the heart in sections near non-excitable tissue like the heart valves or surgery scars. In the second configuration the obstacle is located in the centre of the simulation area to mirror an experiment performed by Ikeda *et al.* [53]. In the first configuration the obstacles centre is chosen as $x_0 = 10$ and by the condition $y_0 = \xi_c + 0.5$ to assure that the influence of the boundary is negligible. An activation wavefront is expected to enter the tissue from the boundary. Hence, an excitation wave is generated by the application of a depolarising current $I = -1$ for a duration t_I at the region $0 < x < 20$, $0 < y < 0.5$. In all cases we chose $t_I = 1$. This yields an action potential, which propagates regularly through the simulation area. This configuration does not generate a spiral wave. The activation wave propagates

symmetrically around the obstacle, enters the tissue behind the obstacle and meets its symmetric counterpart. Since the excitation vanishes if two activation wavefronts collide or one wavefront enters the refractory tail of a previous excitation, no spiral wave occurs. Thus the initial conditions have to be modified to force the excitation wave to propagate only on one side of the obstacle. Therefore the initial values for u and v are chosen inhomogeneously now with $u = 1.6$ and $v = 0.0$ in the region $x > 10$ and $y < 10$, while kept at $u = 1.2$ and $v = 0.6$ in the remaining part. This means that the tissue is in the refractory state initially.

The combination of the results of the phase singularity detection and the manual analysis yields the dynamical phase diagram shown in Figure 27, which is analogous to the phase diagram for the ectopic focus shown in Figure 25. It describes the behaviour of the excitation wave according to the number of circulations around the obstacle depending on ξ_c and Δc.
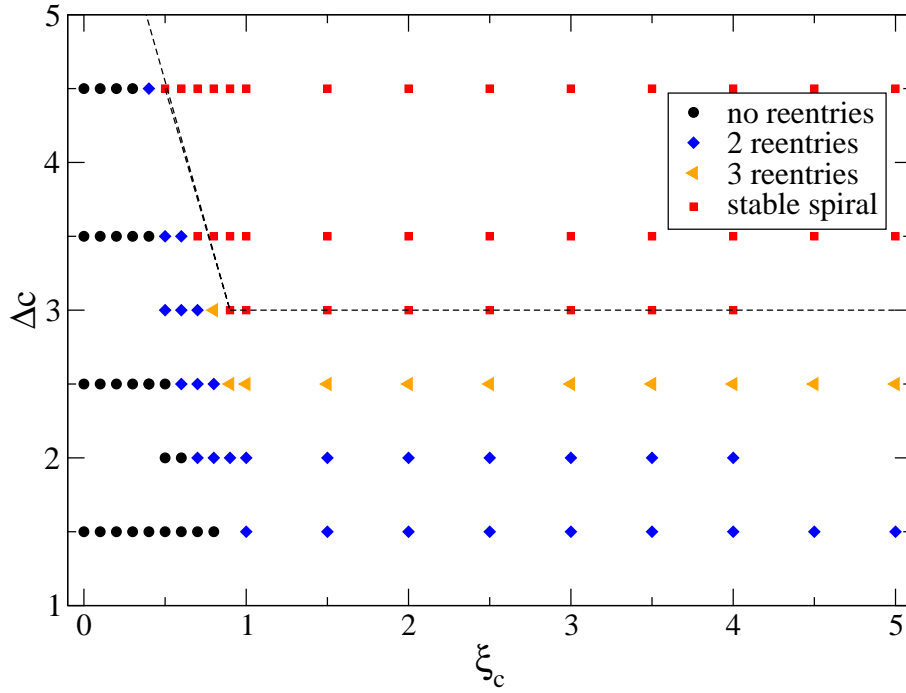

Figure 27: Number of circulations of the excitation wave depending on the obstacle size ξ_c and the difference in excitability Δc. The dashed line marks the region, where stable spiral waves are observed.

As seen in this figure different behaviours are distinguishable. For small obstacle sizes ($\xi_c < 0.4$) the activation wave is not influenced by the obstacle. If the initially refractory tissue returned to the resting state, the excitation activates this region, which leads to a curved wavefront. But the curvature is not sufficiently strong to initiate a circulation. Hence, no spiral wave can be obtained and the excitation simply propagates through the simulation area. In Figure 28 (solid blue line) the time evolution of an initially planar excitation wave perturbed by a small obstacle is shown. Increasing the obstacle size for
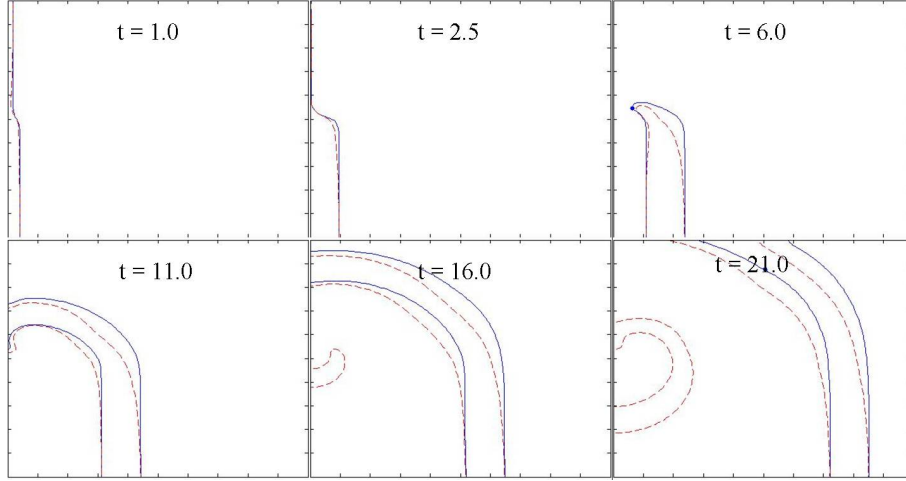
46

Figure 28: Contourplot of the time evolution of variable u for $u_{\text{contour}} = -0.8$, $\Delta c = 3.5$ and two different obstacles sizes $\xi_c = 0.2$ (blue solid lines) and $\xi_c = 2.0$ (red dashed line). Initially the planar excitation wave propagates regularly ($t \lesssim 2.5$). If the initially refractory tissue is excitable, this region is activated and a curved wavefront results ($t \gtrsim 6.0$). For $\xi_c = 0.2$ the curvature of the wavefront is not sufficiently strong to yield a circulation. For $\xi_c = 2.0$ the strong perturbation by the obstacle yields a much more pronounced curvature and thus a stable spiral wave.

a constant Δc yields a stronger perturbation, resulting in a more pronounced curvature of the wavefront. For ξ_c larger than a critical obstacle size of approximately 0.4, the curving of the wave leads to a circulation of the excitation, a reentry. If the reentry radius is too small, the excitation meets its refractory tail and vanishes after two or three circulations. Otherwise a stable circulation, a spiral wave, can develop (red dashed line in Figure 28). If ξ_c is increased beyond $\xi_c = 3.5$ for $\Delta c = 4.5$, a breakup of the spiral wave occurs, due to the strongly decreased excitability of the obstacle, as shown in Figure 29. After some time (approximately $t \approx 32$ for $\xi_c = 5.0$ and $\Delta c = 4.5$) the underlying spiral wave stabilises and the breakup disappears.

Decreasing the difference of the excitability Δc for a certain obstacle size $\xi_c \gtrsim 0.4$ yields a decreased number of circulations of the excitation wave around the obstacle due to the reduced perturbation of the wave by the obstacle. For $\xi_c \approx 0.4$ a transition from a state without circulations ($\Delta c \lesssim 3.5$) to a state with two circulations ($\Delta c \approx 4.5$) is observed. Increasing the obstacle size moves the transition to smaller values of Δc. In addition, stable spiral waves are obtained. For large obstacle sizes $\xi_c \gtrsim 1$ two circulations are obtained for the range $1.5 \lesssim \Delta c \lesssim 2.5$, three circulations for $\Delta c \approx 2.5$, and stable spiral waves for $\Delta c \gtrsim 3$. These transitions are independent of the obstacle size. They are obtained for all values of $\xi_c \gtrsim 1$.

To summarise, for an obstacle size $\xi_c \lesssim 0.4$ no reentry is observed for the physiologically meaningful values of Δc. Increasing the obstacle size yields circulations of the excitation wave, stable spiral waves and finally for $\Delta c \approx 4.5$ spiral wave breakup patterns. A decrease of the difference of excitability Δc
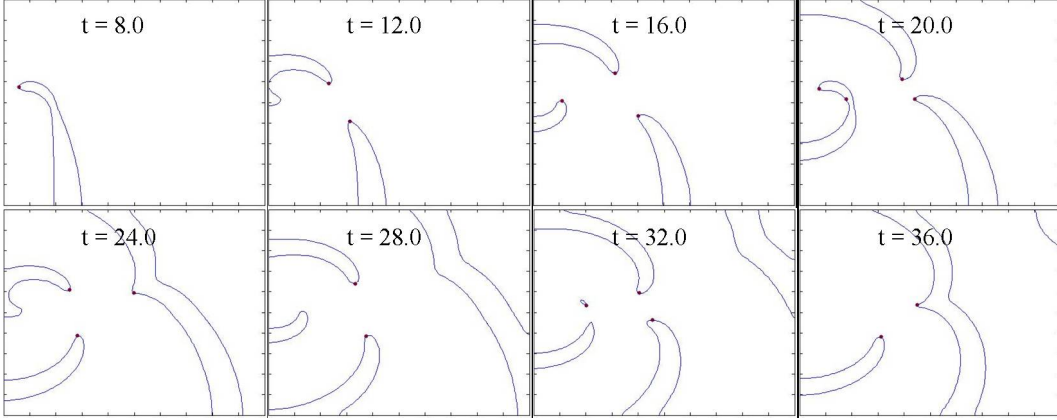
Figure 29: Contourplot of the time evolution of u for $u_{\text{contour}} = -0.8$, $\xi_c = 5.0$ and $\Delta c = 4.5$. The strong perturbation by the obstacles results in a breakup of the waves emanating from the spiral (see the change of pattern from $t = 8.0$ to 12.0 and $t = 20.0$ to 24.0). After some time ($t \gtrsim 32.0$) the spiral stabilises and no breakup is observed anymore for much larger times. The pattern becomes stationary.

results in a decrease of the numbers of reentries to two circulations for $\xi_c \gtrsim 1$, while for $\xi_c \lesssim 0.9$ reentry completely fails. In conclusion, stable spiral waves are obtained in the range of $\xi_c \gtrsim 1$ and $\Delta c \gtrsim 3.0$.

Analysing the path of the phase singularities of the spiral waves reveals, that all spiral waves (without consideration of spirals for $\xi_c \leq 3.5$) are fixed in space and do not move through the simulation area. However, a difference between spirals for $\Delta c \approx 4.5$ and $\Delta c \lesssim 3.5$ is observed, which we describe in more detail next.
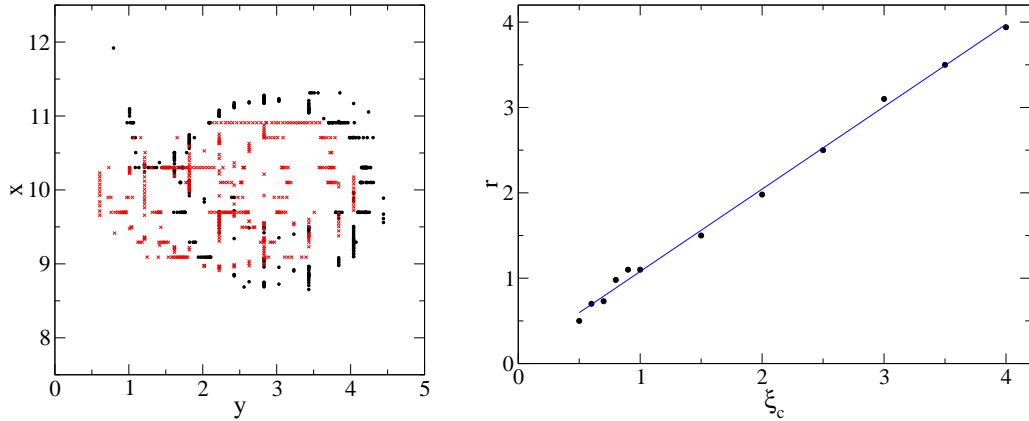

Figure 30: Left panel: Time evolution of phase singularity of spiral waves for $\Delta c = 4.5$ (black dots) and $\Delta c = 3.0$ (red crosses). The black dots prescribe a circle, whereas the pattern of the red diamonds does not prescribe a simple path. Right panel: Dependence of circle diameter r on obstacle size ξ_c for $\Delta c = 4.5$. The diameter is directly proportional to the obstacle size.

In Figure 30 (left graph) the time evolutions of the phase singularities of spi-

rals for $\Delta c = 4.5$ (black curve) and $\Delta c = 3.0$ (red curve) are shown. The phase singularities for $\Delta c = 4.5$ lie approximately on a circle with a diameter r, implying that the spiral wave propagates around the obstacle. The circle diameter r is directly proportional to the obstacle size ξ_c as can be seen in Figure 30 (right graph). For $\Delta c = 3.0$, however, such circle is not obtained, indicating that the tip of the spiral meanders in the region of the obstacle.

To conclude, the spiral wave for $\Delta c = 4.5$ is directly anchored to the obstacle. This phenomenon is known as *anatomical reentry*, where the reentry radius and the fibrillation rate are dependent on the obstacle size. The counterpart is the *functional reentry*, where the fibrillation rate and reentry radius are independent of the obstacle size. In this case, the perturbation by the obstacle creates a pronounced curvature sufficient for circulation, but the size of the obstacle does not influence the properties of the spiral itself like the frequency and reentry diameter.

For an intermediate value $\Delta c = 3.5$, the reentry radius depends only for $\xi_c \lesssim 2.5$ on the obstacle size. Moreover, it takes a longer time for the spiral wave to anchor to the obstacle, i.e. the circular path for the time evolution of the phase singularity is not obtained until $t \approx 25.0$. For $\Delta c = 3.0$ this anchoring is not observed even for very long simulation times ($t \approx 100.0$). Thus, one can conclude that a transition from anatomical reentry for $\Delta c \approx 4.5$ to functional one for $\Delta c \lesssim 3.5$ occurs.

Another evidence for this transition yields the frequency analysis. The frequency in dependence of ξ_c for different values of Δc is shown in Figure 31. For $\Delta c = 4.5$ the frequency of excitation emanating from the spiral wave de-
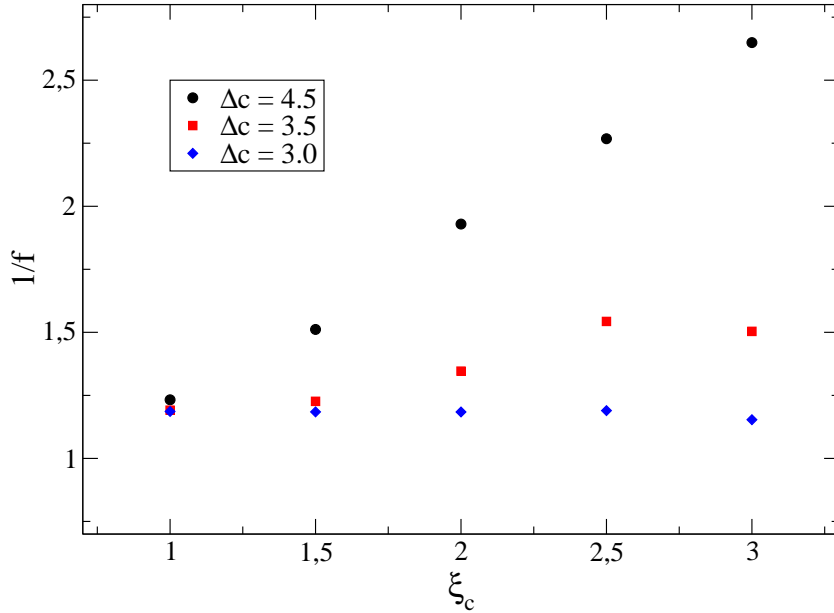

Figure 31: The inverse of frequency of spiral wave in dependence on obstacle size ξ_c for different values of Δc. The frequency of the spiral is inversely proportional to the obstacle size for $\Delta c = 4.5$ and for $\Delta c = 3.5$ up to an obstacle size of $\xi_c \approx 2.5$. For $\Delta c = 3.0$ the reentry frequency is independent of ξ_c.

creases with increasing obstacle size ξ_c. An approximation for the frequency is given by the inverse of the circulation time $\tau \simeq r/v$ with the circle diameter r and the angular conduction velocity v. Since the conduction velocity is constant and $r \sim \xi_c$, $f \sim 1/\xi_c$. On the other hand, for smaller values of Δc the frequency is independent of the obstacle size ξ_c. The different dependencies of the frequency on the obstacle size support the conclusion, that two types of reentry are observed, functional and anatomical reentry.

In the second configuration the obstacles are located in the centre of the simulation area to mirror the experiment performed by Ikeda *et al.* [53]. In this experiment a nearly rectangular area of atrial tissue was placed on a electrode plaque in a tissue bath. Holes with different diameters were created and a reentrant wave was initiated by crossfield stimulation (for a description see section 4). The experimental setup and a section of atrial tissue with a hole is shown in Figure 32. The resulting behaviour of the wavefront was, amongst
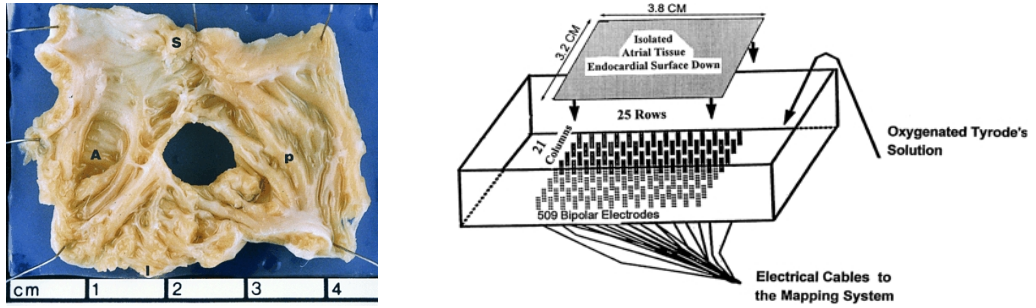

Figure 32: Left panel: A representative section of isolated canine right atrial endo-cardial appendage with its adjacent atrial chamber with a hole of 10 mm diameter. S indicates superior, A appendage, I inferior and P pectinate (from [53]). Right panel: Schematic graph of the electrode plaque mounted on the floor of the tissue bath. The endocardial side of the atrium is mounted on the plaque (from [53]).

others, classified according to, whether the spiral is anchored by the obstacle and by the relationship between hole size and cycle length of the reentry. It was observed, that for large obstacle sizes (6, 8 and 10 mm) the reentrant wave attaches to the obstacle. For smaller obstacle diameters, in contrast, the wave was meandering around it, since the tip of the spiral got variably closer to or further away from the hole.

The missing anchoring for small hole sizes is explained by Ikeda with the source-sink relationship. The sink is increased for smaller obstacles, since a larger number of cells has to be depolarised by the activation wavefront. If the source-sink ratio is decreased below a certain critical ratio, the wavefront detaches from the obstacle. Another result of the experiment is a positive linear correlation between the hole diameter and the cycle length for hole diameters larger than 4 mm. The cycle length is defined as the time interval for one circulation.

For the corresponding set-up in the simulation the following initial state and parameters are used: an obstacle, modelled according to equation (5.3), is located in the middle of the two-dimensional simulation area, i.e. $x_0 = y_0 = 10$,
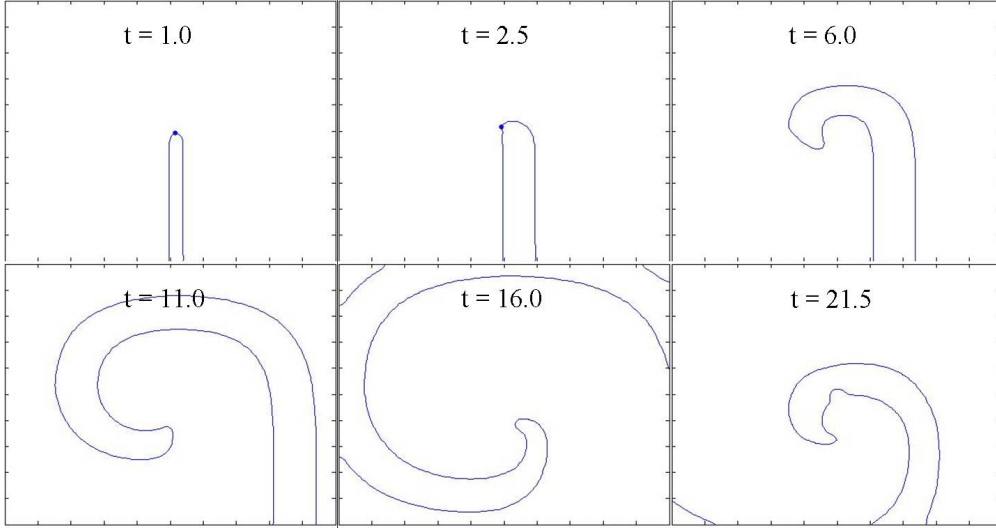
Figure 33: Contourplot of the time evolution of u for $u_{\text{contour}} = -0.8$, $\xi_c = 0.1$ and $\Delta c = 4.5$. The generated excitation, similar to an activation pattern after crossfield stimulation in experiments, results in a spiral wave. The perturbation of the wavefront for $t = 21.5$ reveals the influence of the obstacle.

and a reentrant wave is generated by the application of a current in the region $0 \leq x \leq 10$ and $10 \leq y \leq 10.5$. The tissue behind the wave is in the refractory state initially, i.e. $u(y < 10) = 1.6$ and $v(y < 10) = 0.0$, in order to force the wave to propagate in the positive y direction. This wavefront represents the activation pattern directly after application of a crossfield stimulation. It is reentrant due to the curvature of the wavefront induced by the activation of the excitable tissue in x direction.

In Figure 33 the time evolution of the activation wavefront for an obstacle size of $\xi_c = 0.1$ and difference in excitability of $\Delta c = 4.5$ is shown. One can see, that a spiral wave is obtained. The small perturbation of the wavefront curvature at $t = 21.5$ in the region $x = y = 10$ demonstrates the influence of the obstacle. The difference in excitability of $\Delta c = 4.5$ reflects an almost inexcitable tissue, corresponding to the hole in the experiments. A frequency analysis is performed for different values of the obstacle size ξ_c and the difference in excitability. The results are shown in Figure 34. The mean cycle length measured in the experiments is represented by the inverse of the frequency, calculated in the simulations. An inversely proportionality of the reentry frequency on the obstacle size can be observed for $\xi_c \leq 2.5$ and $\Delta c = 4.5$ and 3.5, in accordance with the experiments. Additionally, for $\xi_c \gtrsim 3.0$ a breakup of the reentrant wave can be observed, which is not found in the experiments. This could be caused by the modified conduction and cell properties and not a direct consequence of the obstacle. This is the reason for the changed frequency dependence for obstacle sizes $\xi_c \gtrsim 3.0$.

For smaller values of Δc ($\Delta c = 2.5$ or 1.5) and obstacle sizes $\xi_c \gtrsim 3.5$ the breakup of the wave leads to a formation of two counter-rotating spiral waves. A transition is observed between a state for $\Delta c \gtrsim 3.5$ ($\xi_c \lesssim 2.5$), where the
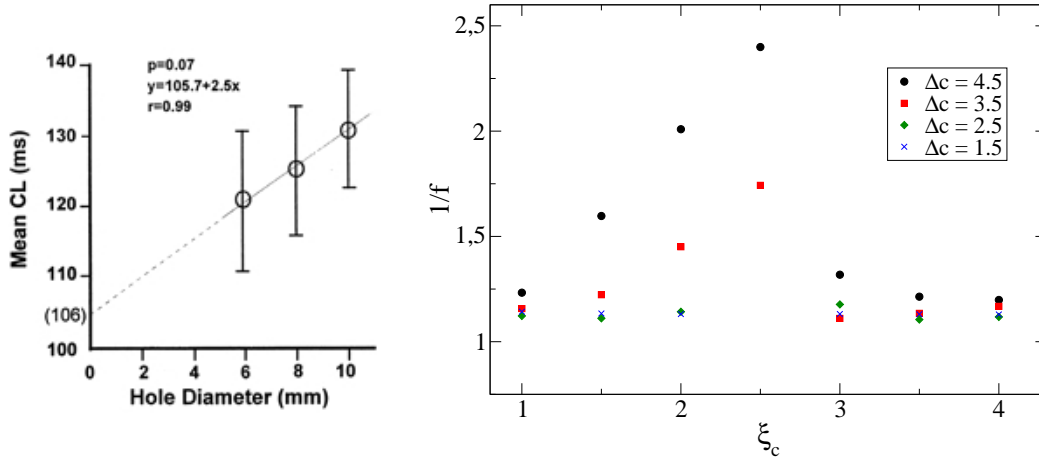
Figure 34: Left panel: Mean cycle length vs. hole diameter measured in the experiment of Ikeda. A positive linear correlation is found. Right panel: Mean cycle length (inverse frequency $1/f$) vs. obstacle size ξ_c calculated from simulation. For $\Delta c = 4.5$ the mean cycle length is approximately inversely proportional to the obstacle size, in agreement with the experiment.

frequency depends on the obstacle size, and a state for $\Delta c < 3.5$, where the frequency is independent of the obstacle size. This is reminiscent of the transition from anatomical to functional reentry, as it was observed for obstacles near the boundary. In contrast to the boundary affected situation, spiral waves are observed here even for small values of ξ_c ($\lesssim 0.5$). On the other hand, the breakup patterns of the wave do not vanish with time for large obstacles. Consequently, a small distance of an obstacle to non-excitable tissue, represented by the boundaries in the simulation, can result in a suppression of reentry for small obstacles and a stabilisation of regular patterns for larger ξ_c. This might be an explanation for termination of atrial fibrillation by catheter ablation, since the cuts, applied near obstacles like the pulmonary veins, represent boundaries as used in the simulations.

5.4   A spiral wave interacting with sinus node excitations

In previous studies [67, 68] the focus of simulations was on the influence of pacing on spiral waves, with the motivation to suggest a possible therapy to suppress fibrillation or tachycardia. In these simulations the pacing was applied to the region, where the spiral wave was located. Davidenko [68] found that the pacing leads to an annihilation of the reentrant activity or to a shift of the spiral core.
In this work the study focuses on the influence of the reentrant activity onto regular paced excitation waves, which represent wavefronts emanating from the sinus node. Thereby, the spiral wave and the sinus node are located in separated regions, which are only connected by a small region. This configuration is based on electrocardiogram recordings and frequency measurements, which exhibit a regular pattern in the left atrium and an irregular one in the

right atrium. In the model, this is represented by a stable pacemaker in the left atrium and normal sinus node excitations in the right. It is shown that the influence of the stable pacemaker yields a fibrillatory state in the right atrium.
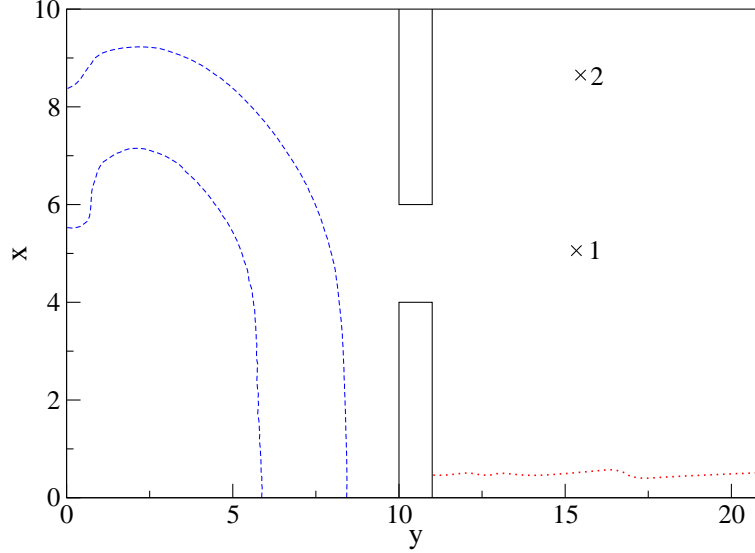

Figure 35: Schematic graph of the simulation area used for the investigation of the interference of a spiral wave with regular planar excitations. The solid black lines represent the von Neumann boundaries. The blue dashed lines are the contour lines for $u = -0.8$ of the spiral wave. The red dotted line represents a excitation wave of the regular pacing. The black crosses (labelled '1' and '2') mark two representative observation sites, where the frequency is measured.

In our numerical calculations the configuration is realised by dividing the simulation area into two rectangular regions linked by a small bridge (see Figure 35). The spiral wave is initiated in the region $0 \leq x, y \leq 10$, which represents the left atrium. It is generated by a planar excitation wave anchoring to an obstacle at $x_0 = 10$ and $y_0 = 1$ of size $\xi_c = 0.5$ and difference of excitability $\Delta c = 4.5$, as described in section 5.3. The circulation time of the spiral wave is approximately 11. Regular planar activation waves are generated after the spiral wave has stabilised ($t = 10$) in the right atrium, represented by the region $11 < x < 21$ and $0 < y < 10$. This is done by the application of a current $I = -1$ with duration $t_I = 1$ in every nth time step in the region $11 \leq x \leq 21$ and $y \leq 0.5$. The frequency of these activations is thus $f_{\text{pace}} = 1/n$. The resulting patterns for different values of the pacing frequency f_{pace} are studied by frequency analysis and manual inspection. The frequency dispersion is specified by taking the average and standard deviation over 16 different points in the right atrium. The results are analysed in terms of the ratio of the pacing frequency f_{pace} to the reentry frequency $f_{\text{spiral}} \approx 1/11.0$ in the left atrium.

For small pacing frequencies ($n \geq 10$) the influence of the activation wavefronts emanating from the spiral onto the regular waves, due to the pacing, is negligible. Small deformations of the regular planar excitation waves can
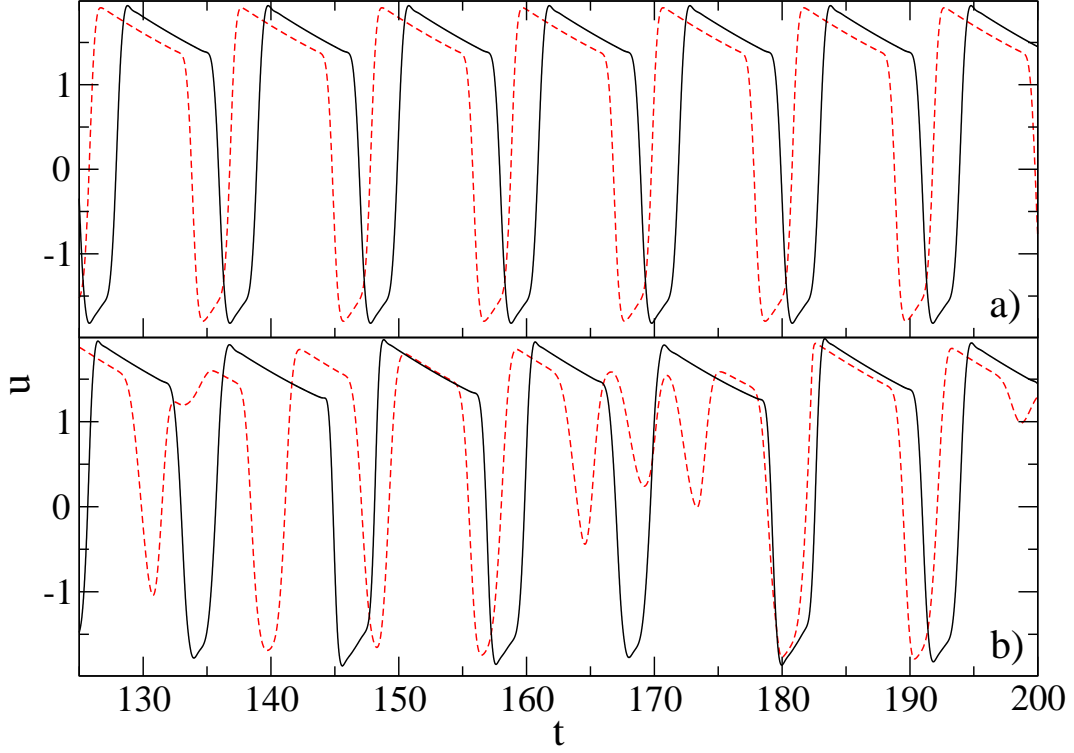
Figure 36: Time evolution of u at observation sites '1' (black solid line) and '2' (red dashed line) (marked in Figure 35) for pacing frequencies a) 0.909 and b) 1.176. A regular pattern analogous to sinus rhythm is observed for the small frequency. In contrast, for the large frequency the time course of u exhibits an irregular pattern, which is similar to fibrillatory patterns in the ECG of AF patients.

be observed, but the measured frequencies resemble approximately the pacing frequency and the overall spatio-temporal pattern of u exhibits a regular pattern (see Figure 36 a). Almost no spatial dispersion of the frequencies is observed ($\sigma_f \simeq 0.005$).

If the pacing frequency is increased, the time evolution of u at the observation sites '1' and '2' (see Figure 35) possesses a strongly changed, irregular pattern similar to those observed in the ECG of patients with atrial fibrillation. In Figure 36 the time evolutions of u for two frequencies (a) $f_{\text{pace}} = 0.909$ and (b) $f_{\text{pace}} = 1.276$ are shown. Two effects are observed for the increased pacing frequency. The shape of the action potential changes if the time interval between two activations is decreased, as seen for observation site '1' (black solid line). In this way, the refractory period shortens as a response to the fastened pacing. This is known as action potential restitution and is a well-known phenomenon of atrial tissue.

As a second effect unsuccessful activations can be observed (red dashed line in Figure 36 b). These result from a breakup of the planar excitation wavefront due to the interference with the spiral wave. This breakup leads to the formation of a second spiral wave seen in the marked area in Figure 37. The spatial variation of the measured frequencies increases by a factor of 100
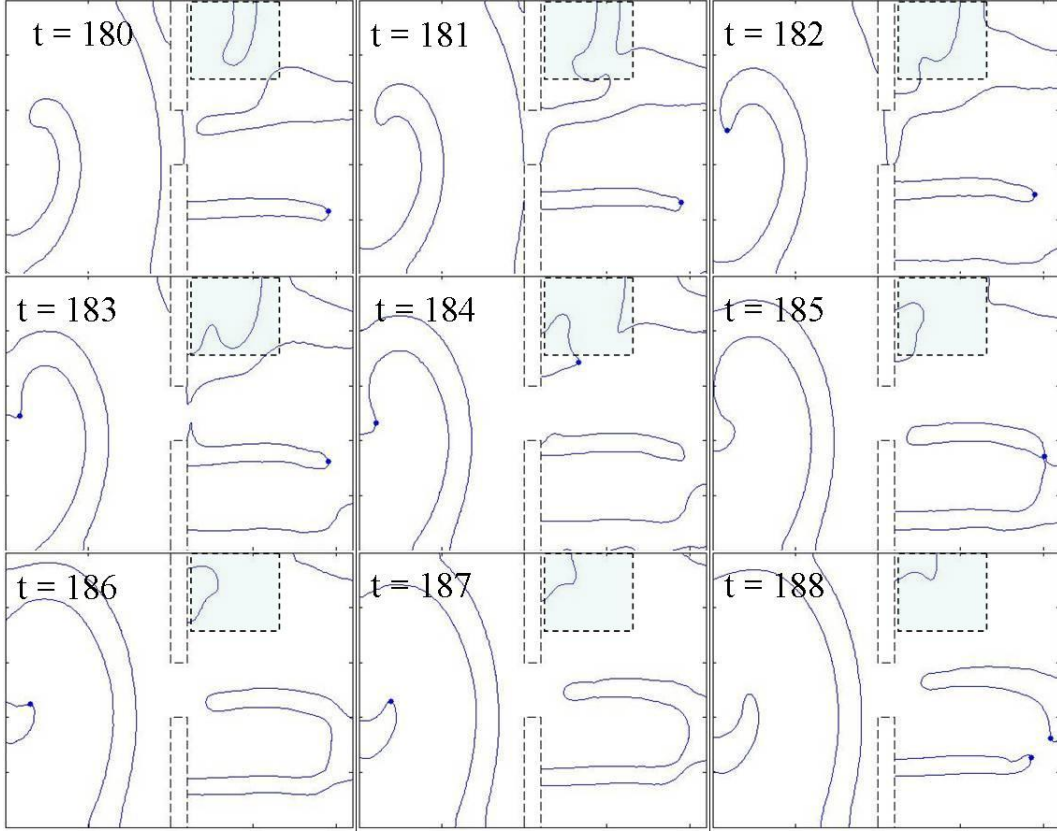
Figure 37: Contourplot of the time evolution of activation variable u (for $u_{\text{contour}} = -0.8$) for interaction of spiral wave with regular pacing at frequency 1.276. The pattern in the right part of the simulation area becomes more irregular with time, whereas the spiral wave in the left part is not influenced. After $t = 180$ the evolution of a spiral wave in the upper left corner of the right part of the simulation area is seen.

($\sigma_f \simeq 0.15$) compared to small pacing frequencies. In some regions the time intervals between consecutive activations are prolonged, because these regions are often passed by activation wavefronts leading to a partial reinitialisation of the refractory period. Thus, no action potentials are generated and the total refractory period is prolonged. In other regions no breakup of waves occurs and consequently a frequency close to the pacing frequency of the sinus node activity is obtained.

To conclude, the interference of the wavefronts emanating from the spiral in the left part of the simulation area with the planar excitation waves, yields an irregular, fibrillatory-like pattern in the right part of the simulation area for large pacing frequencies. The spiral wave in the left part is almost unchanged. Our simulations reveal, that for a relatively large range of pacing frequencies ($0.9 \leq f \leq 1.1$) a regular pattern is observed, and only at the upper limit of reasonable pacing frequencies ($f \simeq 1.28$) the irregularity in the voltage distribution $u(x, y, t)$ emerges. This could be a reason, why the fibrillatory state of the atria is often temporary and provoked by stress.

6 Summary and Outlook

The aim of this work was to answer the four questions given in the introduction. Answers were found by numerical calculations of the well-known FitzHugh Nagumo model (3.28) with different spatial distributions of the parameters and configurations of the simulation area.

The ectopic activity was studied on a two-dimensional squared simulation area with von Neumann boundary conditions. The resting state stability was reduced in circular regions of the tissue by a spatial variation of the parameter b as a model of hyperactive cells. The result of the numerical calculation reveals the possibility to obtain ectopic activity by this mechanism. A minimal size of hyperactive tissue is necessary for ectopic activity as well as a minimal difference of the resting state stability. With increasing size of the hyperactive tissue, the excitation rate increases and saturates. The saturation frequency depends on the parameter b, which controls both the refractory period and the difference of resting state stability. Consequently, if the difference of resting state stability is decreased, the frequency of the ectopic focus decreases.

For the spiral wave patterns it was found that a possible generating mechanism is the anchoring of a planar excitation wave by an obstacle. To uncover this mechanism, an obstacle was modelled as a patch of modified tissue with reduced excitability. This was achieved by a spatial variation of the parameter c in the FHN equations. A planar excitation wave was generated at the boundary and forced to propagate on one side of the obstacle initially, due to inhomogeneous initial conditions with refractory tissue on the other side of the obstacle. As a consequence a circulation of the wave occurs. A dynamical phase diagram was derived, which allows one to distinguish the different behaviours of the activation wave in dependence of the obstacle size and the difference in the excitability. A transition from a state with negligible perturbation of the activation wavefront by the obstacle to a state with a number of circulations of the wave, stable spiral waves or even breakup patterns is observed. In a certain range of obstacle size and difference of excitability, reentry circuits are stable. The spiral waves in this range differ by the dependence of their frequency, reentry path and diameter on the obstacle properties. These properties can become independent of the obstacle size, if the difference of excitability is decreased. This behaviour corresponds to a transition from anatomical to functional reentry as observed in experiments.

A second configuration was studied for a more specific comparison with an experiment, performed by Ikeda *et al.* [53]. The experiment investigated the perturbation of an initially generated reentrant wave by a hole inside a section of canine atrial tissue. This was modelled by an obstacle located in the middle of the two-dimensional square simulation area. A planar excitation wave was generated aside of the obstacle in front of a refractory region, which represents an activation pattern observed after crossfield stimulation in experiments. The modelling shows the emergence of a reentrant wave. Moreover, the analysis of the spiral wave frequency in dependence of the obstacle size yields results in accordance with the experiment. Additionally, for large obstacle sizes breakup of

waves occur that result in irregular activation patterns. These were found also in the boundary affected configuration, but there a transition of the irregular pattern to a stable spiral wave appears. A comparison of the two situations reveals, that a small distance of the obstacle to the boundary stabilises excitation waves interacting with an obstacle. This yields a more stable, regular activation pattern. The von Neumann boundary conditions represent inexcitable tissue as the heart valves or operation scars in the heart. Hence, the observed stabilisation of the activation wave, due to the decreased distance to the boundary, could be an explanation for the termination of atrial fibrillation by catheter ablation. It seems promising to study this effect in more detail by introducing boundaries into the system, representing patterns of scars applied by catheter ablation.

The perturbation of a regular planar excitation in the right atrium by a spiral wave in the left atrium was shown to be a possible generating mechanism for fibrillation in the right atrium. In the modelling of this effect the simulation area was separated into two squared two-dimensional regions connected by a small bridge. A spiral wave was initiated in the left region by anchoring of a planar wave to an obstacle near the boundary, as investigated before. Planar excitation waves were generated by periodic application of a stimulating current at one boundary in the right part of the simulation area with different pacing frequencies. For small pacing frequencies, representing a typical 1 Hz sinus node rhythm, the interference of the spiral wave and the regular pacing is small and (almost) no change of the activation pattern in the right part of the simulation area occurs.

If the frequency is increased, the perturbation by the spiral wave becomes more pronounced and the activation pattern in the right part becomes irregular. The time evolution of the potential u, measured at certain points, exhibits characteristic features, in close resemblance to the ones found in electrocardiogram recordings during fibrillation in the right atrium. Additionally, an increased spatial variation of the excitation frequency in the right part of the simulation area is obtained, emphasising the observed irregularity of the activation pattern. The irregular patterns are observed for high pacing frequencies. This fact can be an explanation, why atrial fibrillation is often provoked by stress, which causes a fastened heart beat. Prospective studies should investigate this effect, for example, by the analysis of activation patterns caused by different distributions of the pacing frequency. This would represent more closely the natural variations of the sinus node rhythm. The frequency is known to depend on the state of health, the stress level and activity status of the patient. Furthermore, a comparison of characteristic properties of simulated Electrocardiograms with ECG recordings from the atria of patients, measured by for example a HALO catheter, should be carried out. Finally, it would be interesting to investigate also the perturbation of regular excitation waves in the right atrium by an ectopic focus in the left atrium.

7 Acknowledgement

8 References

[1] Statistisches Bundesamt Deutschland,
`http://www.destatis.de/jetspeed/portal/cms/Sites/destatis/`
`Internet/DE/Content/Statistiken/Gesundheit/Todesursachen/`
`Tabellen/Content75/SterbefaelleInsgesamt,`
`templateId=renderPrint.psml`, (2007)

[2] A.L. Hodgkin, A.F. Huxley, *A quantitative description of membrane current and its application to conduction and excitation in nerve*, J. Physiol. **117**, 500 (1952).

[3] R. FitzHugh, *Thresholds and plateaus in the Hodgkin-Huxley nerve equations*, J. Gen. Physiol. **43**, 867 (1960).

[4] V. Fuster, L.E. Ryden, D.S. Cannom, H.J. Crijns, A.B. Curtis, K.A. Ellenbogen, J.L. Halperin, J.-Y. Le Heuzey, G.N. Kay, J.E. Lowe, S.B. Olsson, E.N. Prystowsky, J.L. Tamargo, S. Wann, S.C. Smith, A.K. Jacobs, C.D. Adams, J.L. Anderson, E.M. Antman, S.A. Hunt, R. Nishimura, J.P. Ornato, R.L. Page, B. Riegel, S.G. Priori, J.-J. Blanc, A. Budaj, A.J. Camm, V. Dean, J.W. Deckers, C. Despres, K. Dickstein, J. Lekakis, K. McGregor, M. Metra, J. Morais, A. Osterspey, J.L. Zamorano, *ACC/AHA/ESC 2006 guidelines for the management of patients with atrial fibrillation: a report of the American College of Cardiology/American Heart Association Task Force on Practice Guidelines and the European Society of Cardiology Committee for Practice Guidelines (Writing Committee to Revise the 2001 Guidelines for the Management of Patients With Atrial Fibrillation)*, Europace **8**, 651 (2006).

[5] A.S. Go, E.M. Hylek, K.A. Phillips, Y. Chang, L.E. Henault, J.V. Selby, D.E. Singer, *Prevalence of diagnosed atrial fibrillation in adults: national implications for rhythm management and stroke prevention: the AnTicoagulation and Risk Factors in Atrial Fibrillation (ATRIA) Study*, JAMA **285**, 2370 (2001).

[6] W.M. Feinberg, J.L. Blackshear, A. Laupacis, R. Kronmal, R.G. Hart, *Prevalence, age distribution, and gender of patients with atrial fibrillation. Analysis and implications*, Arch. Intern. Med. **155**, 469 (1995).

[7] *Risk factors for stroke and efficacy of antithrombotic therapy in atrial fibrillation. Analysis of pooled data from five randomized controlled trials* [published erratum appears in Arch. Intern. Med. **154**, 2254 (1994)]. Arch. Intern. Med. **154**, 1449 (1994).

[8] `www.texasheartinstitute.org/HIC/Anatomy/conduct.cfm`

[9] R.F. Bosch, J.B. Grammer, V. Kühlkamp, L. Seipel, *Electrical remodeling in atrial fibrillation-cellular and molecular mechanisms*, Z. Kardiol. **89**, 795 (2000).

[10] G. R. Mines, *On circulating excitations in heart muscles and their possible relation to tachycardia and fibrillation*, Proc. Trans. R. Soc. Can. **8**, 43 (1914).

[11] W.E. Garrey, *The nature of fibrillary contraction of the heart-its relation to tissue mass and form*, Am. J. Physiol. **33**, 397 (1924).

[12] T. Lewis, *The mechanism and graphic registration of the heart beat*, 3rd Ed. London, UK: Shaw&Sons, 319 (1925).

[13] S. Nattel, D. Li, L. Yue, *Basic mechanisms of atrial fibrillation-very new insights into very old ideas*, Annu. Rev. Physiol. **62**, 51 (2000).

[14] G.K. Moe, *On the multiple wavelet hypothesis of atrial fibrillation*, Arch. Int. Pharmacodyn. Ther. **140**, 183 (1962).

[15] M.A. Allessie, W.J.E.P. Lammers, F.I.M. Bonke, J. Hollen, *Experimental evaluation of Moe's multiple wavelet hypothesis of atrial fibrillation*, *Cardiac Arrhythmias*, New York, ed. by D.P. Zipes, J. Jalife, 265 (1985).

[16] M. Haisaguerre, P. Jais, D.C. Shah, A. Takahashi, M. Hocini, G. Quiniou, S. Garrigue, A. Le Mouroux, P. Le Métayer, J. Clémenty, *Spontaneous initiation of atrial fibrillation by ectopic beats originating in the pulmonary veins*, N. Engl. J. Med. **339**, 659 (1998).

[17] D. Li, T.K. Leung, S. Nattel, *Mechanisms of atrial fibrillation in dogs with congestive heart failure: electrical remodeling of a different sort*, Circulation **98** (Suppl. 1), I209 (1998).

[18] K. Matsuo, Y. Tomita, K. Uno, C.M. Khrestian, A.L. Waldo, *A new mechanism of sustained atrial fibrillation: studies in the canine sterile pericarditis model*, Circulation **98** (Suppl. 1), I209 (1998).

[19] R. Mandapati, A. Skanes, J. Chen, O. Berenfeld, J. Jalife, *Stable microreentrant sources as a mechanism of atrial fibrillation in the isolated sheep heart*, Circulation **101**, 194 (2000).

[20] J. Chen, R. Mandapati, O. Berenfeld, A.C. Skanes, R.A. Gray, J. Jalife, *Dynamics of wavelets and their role in atrial fibrillation in the isolated sheep heart*, Cardiovasc. Res. **48**, 220 (2000).

[21] A.C. Skanes, R. Mandapati, O. Berenfeld, J.M. Davidenko, J. Jalife, *Spatiotemporal periodicity during atrial fibrillation in the isolated sheep heart*, Circulation **98**, 1236 (1998).

[22] R. Schuessler, *Does size matter?*, J. Cardiovasc. Electrophysiol. **12**, 875 (2001).

[23] P. Jais, M. Haissaguerre, D.C. Shah, S. Chouairi, L. Gencel, M. Hocini, J. Clémenty, *A focal source of atrial fibrillation treated by discrete radiofrequency ablation*, Circ. **95**, 572 (1997).

[24] A. Harada, K. Sasaki, T. Fukushima, M. Ikeshita, T. Asano, S. Yamauchi, S. Tanaka, T. Shoji, *Atrial activation during chronic atrial fibrillation in patients with isolated mitral valve disease*, Ann. Thorac. Surg. **61**, 104 (1996); discussion 111.

[25] T. Sueda, H. Nagata, H. Shikata, K. Orihashi, S. Morita, M. Sueshiro, K. Okada, Y. Matsuura, *Simple left atrial procedure for chronic atrial fibrillation associated with mitral valve disease*, Ann. Thorac. Surg. **62**, 1796 (1996).

[26] J. Sahadevan, R. Kyungmoo, L. Peltz, C.M. Khrestian, R.W. Stewart, A.H. Markowitz, A.L. Waldo, *Epicardial mapping of chronic atrial fibrillation in patients: preliminary observations*, Circulation **110**, 3293 (2004).

[27] P. Sanders, O. Berenfeld, M. Hocini, P. Jais, R. Vaidyanathan, L-F. Hsu, S. Garrigue, Y. Takahashi, M. Rotter, F. Sacher, C. Scavee, R. Ploutz-Snyder, J. Jalife, M. Haisaguerre, *Spectral Analysis identifies sites of high-frequency activity maintaining atrial fibrillation in humans*, Circulation **112**, 789 (2005).

[28] C.A. Morillo, G.J. Klein, D.L. Jones, C.M. Guiraudon, *Chronic rapid atrial pacing: structural, functional, and electrophysiological characteristics of a new model of sustained atrial fibrillation*, Circulation **91**, 1588 (1995).

[29] R. FitzHugh, *Impulses and physiological states in theoretical models of nerve membrane*, Biophys. J. **1**, 445 (1959).

[30] A. Panfilov, R.H. Leldermann, M.P. Nash, *Drift and breakup of spiral waves in reaction-diffusion-mechanics systems*, PNAS **104** (19), 7922 (2007).

[31] A.N. Zaikin, A.M. Zhabotinsky, *Concentration wave propagation in two-dimensional liquid-phase self-oscillating system*, Nature **225**, 535 (1970).

[32] C. J. Weijer, *Dictyostelium morphogenesis*, Current Opinion in Genetics & Development **14** (4), 392 (2004).

[33] A. Malevanets, R. Kapral, *Microscopic model for FitzHugh-Nagumo dynamics*, Phys. Rev. E **55** (5), 5657 (1997).

[34] R. Plonsey, R.C. Barr, *Bioelectricity: a quantitative approach*, Kluwer Academic (2000).

[35] Y. Jiang, A. Lee, J. Chen, V. Ruta, M. Cadene, B.T. Chait, R. MacKinnon, *X-ray structure of a voltage-dependent K^+ channel*, Nature **423**, 33 (2003).

[36] Y. Jiang, V. Ruta, J. Chen, A. Lee, R. MacKinnon, *The principle of gating charge movement in a voltage-dependent K^+ channel*, Nature **423**, 42 (2003).

[37] R. FitzHugh, *Mathematical models of threshold phenomena in the nerve membrane*, Bull. Math. Biophysics **17**, 257 (1955).

[38] L.F. Abbott, T.B.Kepler, *Model neurons: from Hodgkin-Huxley to Hopfield*, Statistical Mechanics of Neural Networks (Springer-Verlag, Berlin, 1990), p. 5.

[39] G.R. Mines, *On dynamic equilibrium in the heart*, J. Physiol. **46**, 349 (1913).

[40] W.E. Garrey, *Auricular fibrillation*, Physiol. Rev. **4**, 215 (1924).

[41] M.A. Allessie, F.I.M. Bonke, F.J.G. Schopman, *Circus movement in rabbit atrial muscle as a mechanism of tachycardia. III. The 'leading circle' concept: a new model of circus movement in cardiac tissue without the involvement of an anatomic obstacle*, Circ. Res. **41**, 9 (1977).

[42] N. Wiener, A. Rosenblueth, *The mathematical formulation of the problem of conduction of impulses in a network of connected excitable elements, specifically in cardiac muscle*, Arch. Inst. Cardiol. **16**, 205 (1946).

[43] A.M. Pertsov, J.M. Davidenko, R. Salomonsz, W.T. Baxter, J. Jalife, *Spiral waves of excitation underlie reentrant activity in isolated cardiac muscle*, Circ. Res. **72**, 631 (1993).

[44] A.S. Mikhailov, V.A. Davydov, V.S. Zykov, *Complex dynamics of spiral waves and motion of curves*, Physica D **70**, 1 (1994).

[45] P.L. Rensma, M.A. Allessie, W.J.E.P. Lammers, F.I.M. Bonke, M.J. Schalij, *Length of excitation wave and susceptibility to reentrant atrial arhythmias in normal conscious dogs*, Circ. Res. **62**, 395 (1988).

[46] S. Nattel, G. Bourne, M. Talajic, *Insights into mechanisms of antiarrhythmic drug action from experimental models of atrial fibrillation*, J. Cardiovasc. Electrophysiol. **8**, 469 (1997).

[47] T. Ikeda, T. Uchida, D. Hough, J.J. Lee, M.C. Fishbein, W.J. Mandel, P.-S. Chen, H.S. Karagueuzian, *Mechanism of spontaneous termination of functional reentry in isolated canine right atrium. Evidence for the presence of an excitable but non excited core*, Circulation **94**, 1962 (1996).

[48] A.V. Holden, *A last wave from the dying heart*, Nature **392**, 20 (1998).

[49] R.A. Gray, A.M. Pertsov, J. Jalife, *Spatial and temporal organization during cardiac fibrillation*, Nature **392**, 75 (1998).

[50] P. Comtois, J. Kneller, S. Nattel, *Of circles and spirals: Bridging the gap between the leading circle and spiral wave concepts of cardiac reentry*, Europace **7**, S10 (2005).

[51] Z.Y. Lim, B. Maskara, F. Aguel, R. Emokpae Jr., L. Tung, *Spiral wave attachment to millimeter sized obstacles*, Circulation **114**, 2113 (2006).

[52] A.T. Winfree, *Varieties of spiral wave behaviour: an experimentalists approach to the theory of excitable media*, Chaos **1** (3), 303 (1991).

[53] T. Ikeda, M. Yashima, T. Uchida, D. Hough, M.C. Fishbein, *Attachment of meandering reentrant wave fronts to anatomic obstacles in the atrium. Role of obstacle size*, Circ. Res. **81**, 753 (1997).

[54] T.J. Wu, M. Yashima, F. Xie, C.A. Athill, Y.H. Kim, *Role of pectinate muscle bundles in the generation and maintenance of intra-atrial reentry. Possible implications for the mechanism of conversion between atrial fibrillation and atrial flutter*, Circ. Res. **83**, 448 (1998).

[55] F. Xie, Z. Qu, A. Garfinkel, *Dynamics of reentry around a circular obstacle in cardiac tissue*, Phys. Rev. E **58**, 6355 (1998).

[56] R.A. Gray, J. Jalife, *Ventricular fibrillation and atrial fibrillation are two different beasts*, Chaos **8** (1), 65 (1998).

[57] A.M. Pertsov, E.A. Ermakova, A.V. Panfilov, *Rotating spiral waves in a modified Fitz-Hugh-Nagumo model*, Physica D **14**, 117 (1984).

[58] S. Nattel, *New ideas about atrial fibrillation 50 years on*, Nature **415**, 219 (2002).

[59] J. Kneller, R. Zou, E.J. Vigmond, Z. Wang, L.J. Leon, S. Nattel, *Cholinergic atrial fibrillation in a computer model of a two-dimensional sheet of canine atrial cells with realistic ionic properties*, Circ. Res. **90**, 73 (2002).

[60] R. Zou, J. Kneller, L.J. Leon, S. Nattel, *Development of a computer algorithm for the detection of phase singularities and initial application to analyze simulations of atrial fibrillation*, Chaos **12** (3), 764 (2002).

[61] S. Iravanian, Y. Nabutovsky, C-R. Kong, S. Saha, N. Bursac, L. Tung, *Functional reentry in cultured monolayers of neonatal rat cells*, Am. J. Physiol. Heart Circ. Physiol. **285**, H449 (2003).

[62] T. Ikeda, L. Czer, A. Trento, C. Hwang, J.J.C. Ong, D. Hough, M.C. Fishbein, W.J. Mandel, H.S. Karagueuzian, P.-S. Chen, *Induction of meandering functional reentrant wave front in isolated human atrial tissues*, Circulation **96**, 3013 (1997).

[63] http://www.mathworks.com/access/helpdesk/help/pdf_doc/pde/pde.pdf

[64] W.R. Gibbs, *Computation in modern physics*, World Scientific Publishing (1999).

[65] M-A. Bray, J.P. Wikswo, *Use of topological charge to determine filament location and dynamics in a numerical model of scroll wave activity*, IEEE Trans. Biomed. Eng. **49** (10), 1082 (2002).

[66] A.N. Iyer, R.A. Gray, *An experimentalist's approach to accurate localization of phase singularities during reentry*, Ann. Biomed. Eng. **29**, 47 (2001).

[67] G.V. Obisov, A.T. Stamp, J.J. Collins, *Suppressing arrhythmias in cardiac models with overdrive pacing*, Control of Oscillations and Chaos (Proc.) **3**, 453 (2000).

[68] J.M. Davidenko, R. Salomonsz, A.M. Pertsov, W.T. Baxter, J. Jalife, *Effects of pacing on stationary reentrant activity*, Circ. Res. **77**, 1166 (1995).